

Article

NLFEA of Reinforced Concrete Corbels: Proposed Framework, Sensibility Study, and Precision Level

Luan Reginato ^{1,2}, Alex M. D. de Sousa ^{1,*}, João V. C. Santos ¹ and Mounir K. El Debs ¹

¹ São Carlos School of Engineering, University of São Paulo, São Carlos 13566-590, SP, Brazil; luanreginato@usp.br (L.R.); joao.caldas@usp.br (J.V.C.S.); mkdebs@sc.usp.br (M.K.E.D.)

² Itaipu Technological Park Foundation (CEASB/PTI), Foz do Iguaçu 85867-900, PR, Brazil

* Correspondence: alex_dantas@usp.br

Abstract: Non-linear finite element analysis (NLFEA) has been frequently used to assess the ultimate capacity of reinforced concrete (RC) structures under the most complex conditions. Nevertheless, the guidelines using such methods to evaluate RC corbels are limited. In addition, the influence of material modeling options regarding the behavior of such members was not investigated until now. This paper proposes to present a framework for the NLFEAs of RC corbels using the Concrete Damaged Plasticity (CDP) model. The influence of several modeling choices related to this constitutive model also is discussed in detail, including the assumed stress–strain behavior in compression and tension and the parameters related to the yield criterion and flow rule. For this, a first set of test results was used to validate the proposed approach to the NLFEA. Afterwards, the sensibility of the numerical results for several modeling choices was investigated. In the end, the proposed framework for the NLFEA was checked against a database of 36 test results from the literature. The mean ratio between the predicted and experimental test results was 1.015 with a coefficient of variation of only 8.57%. The governing failure mechanism of the tests was predicted correctly in approximately 88% of the simulations. In summary, the proposed approach allows for predicting the ultimate capacity and failure mechanism of RC corbels accurately.

Keywords: reinforced concrete corbels; non-linear finite element analysis; concrete damaged plasticity model; numerical modeling



Citation: Reginato, L.; de Sousa, A.M.D.; Santos, J.V.C.; El Debs, M.K. NLFEA of Reinforced Concrete Corbels: Proposed Framework, Sensibility Study, and Precision Level. *Buildings* **2023**, *13*, 1874. <https://doi.org/10.3390/buildings13071874>

Academic Editor: Abdelhafid Khelidj

Received: 28 June 2023
Revised: 17 July 2023
Accepted: 18 July 2023
Published: 24 July 2023



Copyright: © 2023 by the authors. Licensee MDPI, Basel, Switzerland. This article is an open access article distributed under the terms and conditions of the Creative Commons Attribution (CC BY) license (<https://creativecommons.org/licenses/by/4.0/>).

1. Introduction

The use of non-linear finite element analysis (NLFEA) has increased in the last years to assess the ultimate capacity of reinforced concrete (RC) structures under the most complex boundary conditions, and existing structures are preliminary rated as resistance-deficient in most conservative analytical calculations [1–3]. In other words, NLFEA is frequently employed to consider the several non-linearities of a given problem and sometimes hidden capacities not directly addressed in the analytical calculation models. RC corbels are one of these members that sometimes require evaluation via NLFEA. Figure 1 depicts a reinforced concrete corbel and some of the associated definitions. Particularly, reinforced concrete corbels are structural members that frequently attract greater attention in the design and assessment of existing structures due to the different possible failure mechanisms [4,5]: (i) yielding of the primary/main reinforcement (Figure 2a); crushing of the inclined compression strut (Figure 2b,c); and (ii) sliding shear at the column–corbel interface (Figure 2d).

Although the number of studies related to the non-linear finite element analysis of RC corbels increased in the last years [6–10], the following limitations can be identified.

- Firstly, most previous studies were conducted using material constitutive models other than the Concrete Damaged Plasticity model (CDP), such as the total strain fixed or rotating cracking models. Therefore, it is unclear if modeling choices validated from other material models could be extended to the CDP model.

In addition to that, the influence of different modeling choices regarding the stress–strain behavior model and damage evolution models assumed for the concrete was not discussed in the publications [11,12].

- In the same way, the influence of considering the elastic modulus degradation (damage evolution) in the ultimate capacity of RC corbels or not is generally not addressed. In fact, the proposed modeling approaches in the literature were frequently validated against specific experimental programs or a specific failure mechanism. Therefore, it is unclear if the presented modeling choices can be directly extended to simulate other RC corbels under the most complex boundary conditions, for which the governing failure mechanism may differ from that observed in the calibration process.

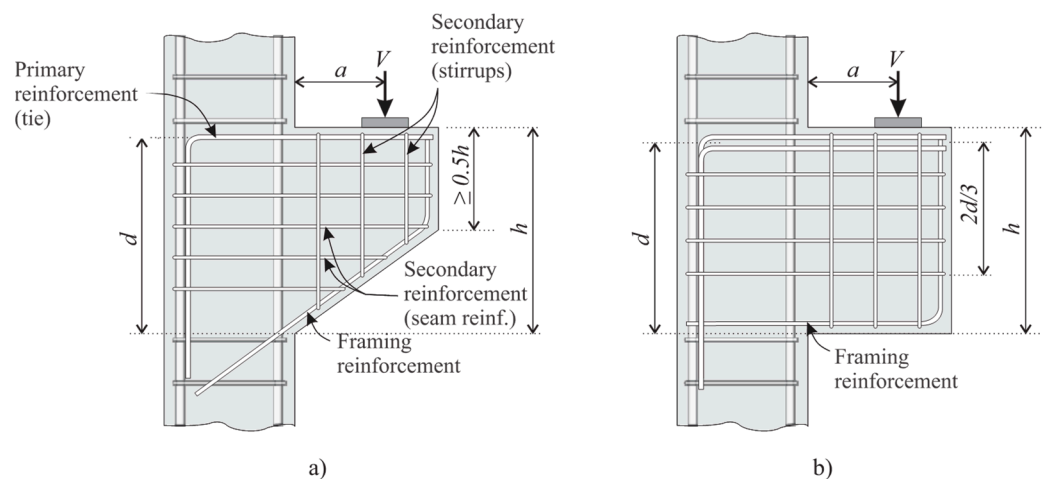


Figure 1. Typical reinforcement arrangement for corbels: (a) with chamfer; (b) without chamfer.

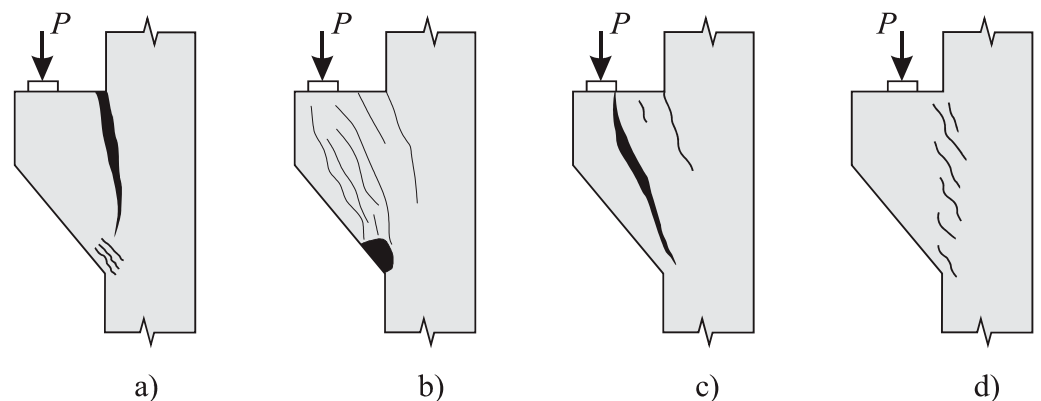


Figure 2. Types of failure in corbels: (a) tensile; (b,c) compression; (d) shear.

This paper intends to discuss the influence of some modeling choices related to concrete behavior in the ultimate capacity and failure mechanism of RC corbels. Herein, the influence of the following parameters is investigated in detail: (i) the stress–strain behavior in compression; (ii) the stress–strain behavior in tension; (iii) the damage evolution laws in tension and compression; (iv) the plasticity parameters of the constitutive model; and (v) the mesh size. In the end, the proposed modeling approach is extended to a database of 36 test results from different references. Therefore, this paper presents a modeling approach validated against a comprehensive range of test results, including different failure mechanisms.

Firstly, we review the different modeling choices that need to be defined in the Concrete Damaged Plasticity model regarding concrete modeling (Section 2). After that, the control tests from the literature used in the sensitivity analyses are described (Section 3). The proposed modeling approach is described in Section 4 and validated for the first group

of test results in Section 5 regarding the load-deflection graphs, ultimate capacity, and cracking pattern (failure mechanism). In Section 6, a sensitivity study is presented to show how some modeling choices from the concrete influence the structural behavior of the evaluated corbels, highlighting some recommendations for the NLFEA of such members. In Section 7, the level of accuracy of the proposed modeling approach using CDP is verified against 36 test results from the literature.

2. Background of the Concrete Damaged Plasticity Model

The Concrete Damaged Plasticity model (CDP) was the constitutive model adopted in this study to represent concrete behavior. In practice, CDP combines the damage and plasticity theories and is grounded on three main aspects:

- (i) Stress–strain behavior models (including damage evolution): models that express the behavior of the yield criterion with the evolution of plastic deformation (uniaxial and triaxial behavior).
- (ii) Yield criterion: indicates (through the stress tensor) the stress level at which the plastification or yielding of the material will occur (the geometric representation of this is commonly called a failure surface);
- (iii) Plastic flow /flow rule: the law that defines the evolution of plastic strains according to the stress level after the yield criterion is achieved.

2.1. Stress–Strain Behavior Models: Hardening/Softening Law

The Concrete Damaged Plasticity (CDP) model available in Abaqus 6.14 © software was used in this study. This model combines the theory of plasticity and the mechanics of continuous damage; it was proposed by Lubliner et al. [13] and incorporates modifications proposed by Lee and Fenves [14]. In uniaxial loads, the stress–strain relationship of concrete can be represented by Figure 3a for tensile stresses and Figure 3b for compressive stresses. The solid line represents monotonic loading, and the dashed line represents unloading or cyclic loading.

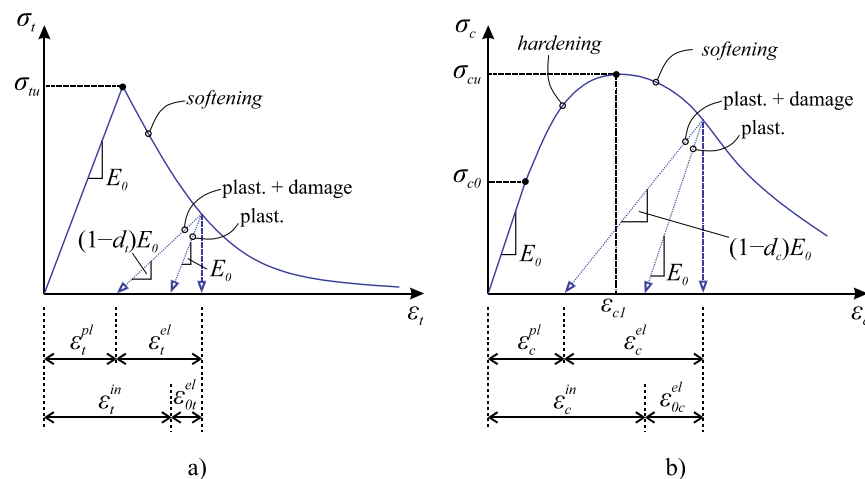


Figure 3. Stress–strain relationship: (a) traction; (b) compression of concrete.

In a monotonic tensile load, a linear elastic regime can be considered until the ultimate failure stress (σ_{tu}), which is caused by cracks in the material. In the plastic regime, the opening of these cracks causes a decrease in stress with increasing deformation, characterizing the softening curve (Figure 3a). For compressive loading, the linear regime can be considered up to the stress σ_{c0} and, with the propagation of microcracks already present in the concrete, there is a decrease in the modulus of elasticity up to the ultimate stress (σ_{cu}) of failure, characterizing the hardening curve (hardening) in plastic regime. Then, as in tension, there is a reduction in stress with increasing deformation (softening) due to the increase and propagation of cracks (Figure 3b).

For unloading or cyclic loads, when considering only the theory of plasticity, elastic return is observed (ε_{0t}^{el} and ε_{0c}^{el} , Figure 3) with the same initial modulus of elasticity E_0 and irreversible or residual strains, defined here as inelastic strains (ε_t^{in} and ε_c^{in} in tension and compression, respectively). With the introduction of the mechanics of the damage, it is possible to consider the elastic stiffness degradation through the parcel $(1 - d_c$ or $1 - d_t)$ that multiplies the initial modulus of elasticity E_0 ; d_c and d_t are the damage variables that vary from 0 (no degradation) to 1 (completely degraded), and the indices t and c correspond to tensile and compressive stresses, respectively. In the material, this degradation occurs due to the accentuated level of cracks present in the concrete plastic stage.

With this, the stress–strain relationship of a uniaxial loading for CDP can be written as [15]:

$$\sigma_t = (1 - d_t)E_0(\varepsilon_t - \varepsilon_t^{pl}) \quad (1)$$

$$\sigma_c = (1 - d_c)E_0(\varepsilon_c - \varepsilon_c^{pl}) \quad (2)$$

For a bi/triaxial state, the stress–strain relationship is given as:

$$\sigma = (1 - d)D_0^{el} : (\varepsilon - \varepsilon^{pl}) \quad (3)$$

where D_0^{el} is the elastic stiffness tensor, σ is the stress tensor, ε is the strain tensor, and d is the scalar damage variable with the same function as the uniaxial case (but now defined together with a multiaxial weight factor).

2.2. Yield Criterion

In CDP, the yield criterion developed by Lubliner et al. [13] with modifications by Lee and Fenves [14] is given as the function F . In terms of effective stresses, the yield criterion takes the following form [16]:

$$\frac{1}{1 - \alpha} \left(\sqrt{3}J_2 + \alpha I_1 + \beta \langle \bar{\sigma}_{\max} \rangle - \gamma \langle \bar{\sigma}_{\max} \rangle \right) = c \quad (4)$$

with:

$$I_1 = \sigma_1 + \sigma_2 + \sigma_3 \quad (5)$$

$$J_2 = -(1/6) \left[(\sigma_1 - \sigma_2)^2 + (\sigma_2 - \sigma_3)^2 + (\sigma_3 - \sigma_1)^2 \right] \quad (6)$$

where α , β , and γ are material parameters that can be calculated as:

$$\alpha = \frac{(\sigma_{bu}/\sigma_{cu}) - 1}{2(\sigma_{bu}/\sigma_{cu}) - 1}; \beta = \frac{\sigma_{cu}}{\sigma_{tu}}(1 - \alpha) - (1 + \alpha); \gamma = \frac{3(1 - K_c)}{2K_c - 1} \quad (7)$$

$\langle \cdot \rangle$ is the Macauley bracket used to distinguish when $\bar{\sigma}_{\max} > 0$ or $\bar{\sigma}_{\max} < 0$ and is given as the following expression: $\langle x \rangle = \frac{1}{2}(|x| + x)$; that is, when $\bar{\sigma}_{\max} > 0$, the Macauley bracket returns the value of x , and for $\bar{\sigma}_{\max} < 0$, the Macauley bracket returns a null value;

σ_{bu} and σ_{cu} are the equibiaxial compressive yield stress and uniaxial compressive yield stress, respectively; σ_{tu} is the uniaxial tensile yield stress and $\bar{\sigma}_{\max}$ is the maximum effective principal stress. The effective stress $\bar{\sigma}$ for tensile and compressive stresses is calculated as:

$$\bar{\sigma}_t = \frac{\sigma_t}{(1 - d_t)} \text{ and } \bar{\sigma}_c = \frac{\sigma_c}{(1 - d_c)} \quad (8)$$

K_c is the ratio of the tensile to the compressive meridian and defines the shape of the yield surface in the deviatoric plane [11]. In the case of a tensile stress state ($\bar{\sigma}_{\max} > 0$), equation F becomes:

$$\frac{1}{1 - \alpha} \left(\sqrt{3}J_2 + \alpha I_1 + \beta \bar{\sigma}_{\max} \right) = c \quad (9)$$

For a biaxial compressive stress state ($\bar{\sigma}_{max} = 0$), the yield function becomes:

$$\frac{1}{1-\alpha} \left(\sqrt{3J_2} + \alpha I_1 \right) = c \quad (10)$$

In a triaxial compressive stress state ($\bar{\sigma}_{max} < 0$), the yield function is:

$$\frac{1}{1-\alpha} \left(\sqrt{3J_2} + \alpha I_1 + \gamma \bar{\sigma}_{max} \right) = c \quad (11)$$

Figure 4 shows the geometric representation of the yield criterion (failure surface) in the plane state of stresses (Figure 4a) and in the deviatoric place (Figure 4b).

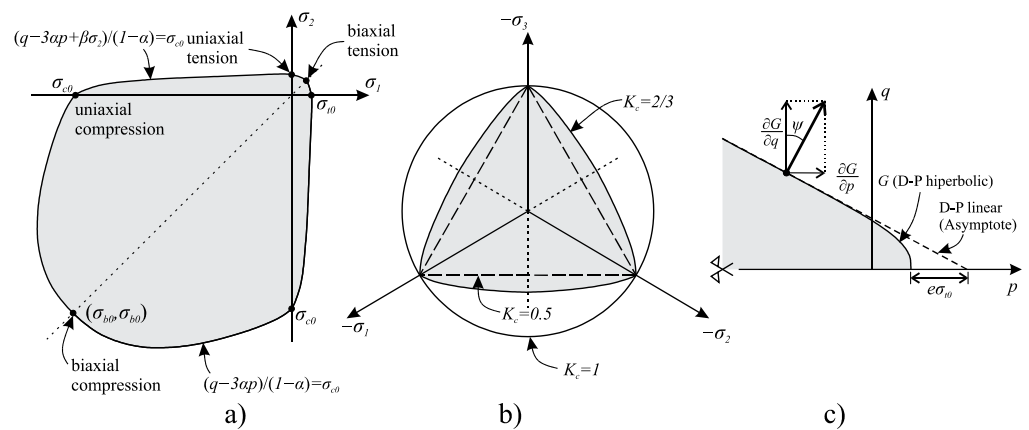


Figure 4. CDP failure surface in (a) stress plane state and (b) deviatoric plane; (c) plastic potential function, dilation angle, and eccentricity in meridian plane p - q .

2.3. Plastic Flow Rule

The plastic flow or flow rule is given as the function G , also called the plastic potential. In CDP, the plastic potential is assumed in a non-associative form, i.e., $G \neq F$. The plastic potential G adopted in CDP is the hyperbolic Drucker–Prager function:

$$G = \sqrt{(e\sigma_{t0} \tan \psi)^2 + \bar{q}^2} - \bar{p} \tan \psi \quad (12)$$

where p and q are the equivalent effective stresses and hydrostatic stresses, respectively; e is the eccentricity that defines the rate at which the function approaches the asymptote; σ_{t0} is the uniaxial tensile stress; and ψ is the dilation angle measured in the p - q plane at high confining pressures (Figure 4c).

2.4. Summary of Input Parameters Required in CDP

In summary, the elastic and plastic input parameters needed to define the constitutive Concrete Damaged Plasticity (CDP) model are:

- E_c —concrete elastic modulus and ν —Poisson coefficient;
- $\sigma_t \times \varepsilon_t^{in}$ and $\sigma_c \times \varepsilon_c^{in}$: uniaxial stress—inelastic strain relationship of concrete in tension and compression;
- $d_t \times \varepsilon_t^{in}$ and $d_c \times \varepsilon_c^{in}$: damage—inelastic strain relationship of concrete to tension and compression;
- σ_{bu}/σ_{cu} : ratio between biaxial and uniaxial compressive yield strengths;
- K_c —shape factor and e —eccentricity;
- ψ —dilation angle and μ —viscosity.

The uniaxial stress–strain relationships, including the damage evolution laws, can be obtained experimentally from instrumented uniaxial static and cyclic tests. On the other hand, measuring other parameters such as σ_{bu}/σ_{cu} , ψ , and K_c requires using biaxial and

triaxial characterization tests to be determined more precisely [12,16,17]. As most of these parameters are not determined in ordinary characterization tests (in practice, only the compressive and splitting tensile strengths are measured in regular tests), the parameters from CDP are frequently determined based on analytical expressions from the literature or calibration studies of the numerical models. Nevertheless, it is important to highlight that these parameters have a physical meaning and, hence, calibration studies should be performed carefully to avoid unrealistic values of parameters. The parameter of CDP that is defined only numerically is the viscosity, which serves to overcome convergence issues from quasi-brittle materials. However, using inappropriate values for this parameter may lead to undesirable material behavior changes in the numerical simulations, as will be shown in the following sections.

3. Control Tests for Modeling

The experimental models chosen for calibrating the numerical models were those documented by Wilson et al. [4]. In this study, four double corbels identified as C0, C1, C2, and C3 (shown in Figure 5) that were designed using the strut-and-tie model (STM) and the empirical method recommended by ACI 318:2014 [18] were tested.

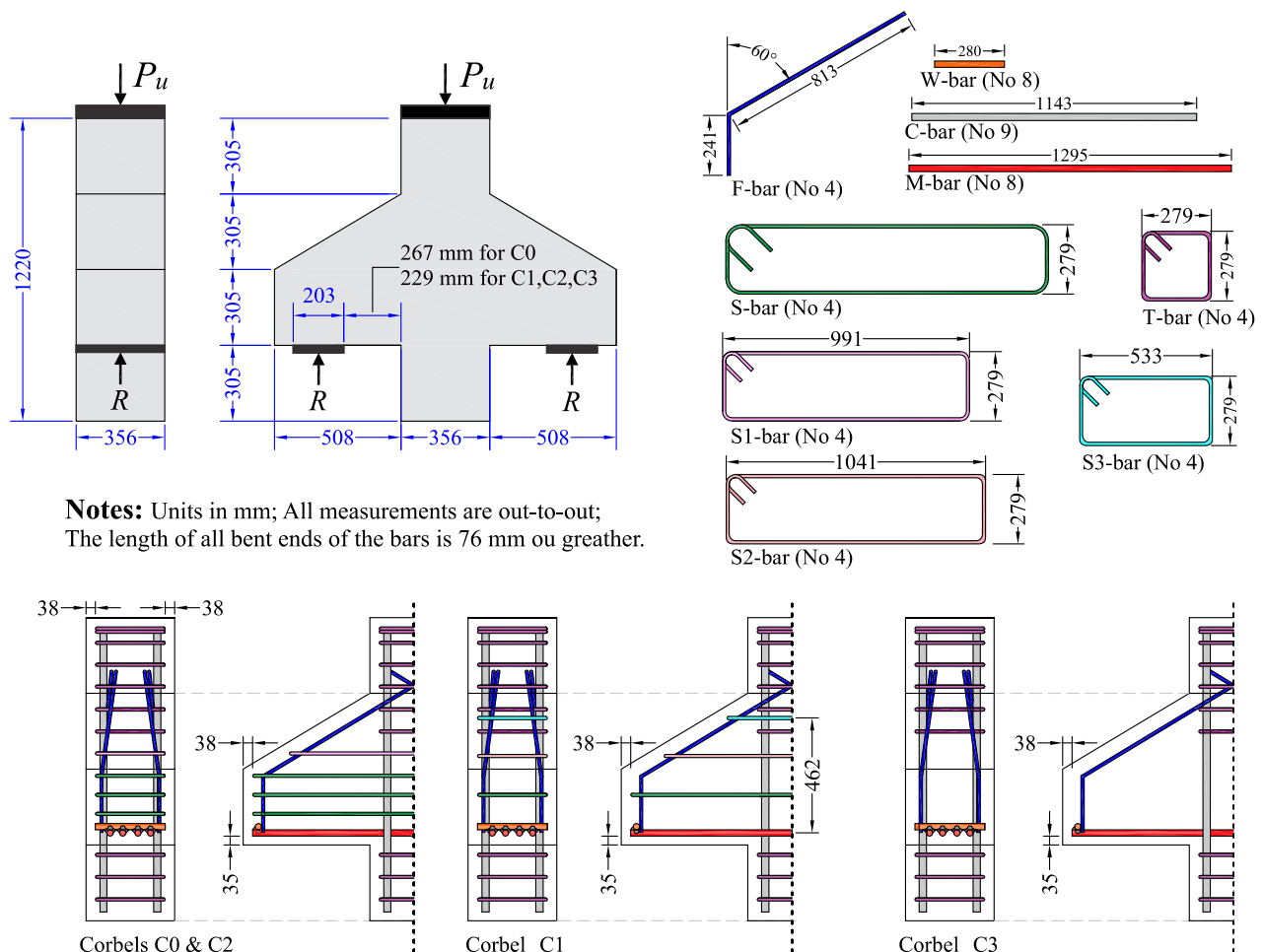


Figure 5. Geometry and reinforcement configurations of the corbels tested by Wilson et al. [4].

The adopted geometry was the same for all corbels as follows: internal height or corbel height (h_{int}) of 610 mm, external height (h_{ext}) of 305 mm, corbel width (b_w) of 356 mm, corbel length (c) of 508 mm, and extended column height (b_{col}) of 305 mm.

Based on the design created by Wilson et al. [4], the primary/tie reinforcement was the same for all corbels, resulting in 4 bars with a diameter of 25.4 mm (Bar M) and effective depth (d) of 559 mm. This reinforcement was anchored at its end through welded transverse

bars of the same diameter (W Bar). As for the horizontal secondary reinforcement, in the C0 and C2 brackets, the same quantity and arrangement were used, with 4 bars in the form of horizontal stirrups with a diameter of 12.7 mm arranged in the first 2/3 of the effective depth from the tie reinforcement (Bars S and S1).

For the C1 corbel, crack control reinforcement was employed (secondary reinforcement) with 3 bars in the form of horizontal stirrups with a diameter of 12.7 mm evenly distributed along the height of the corbel (Bars S, S2, and S3). As for the C3 corbel, no secondary reinforcement was used. In the columns, 4 bars with a diameter of 28.58 mm (Bar C) and horizontal stirrups with a diameter of 12.7 mm (Bar T) were assembled to prevent premature failure of the columns. Finally, a framing reinforcement (Bar F) was placed along the chamfer to ensure the reinforcements' positions.

Each corbel was instrumented with electrical resistance strain gauges in all reinforcements of the tie to monitor the evolution of reinforcement strains during the test; for the braces C0, C1, and C2, the secondary reinforcements were instrumented alternately. The positions of the extensometers/strain gauges coincided with the interface between the corbel and the columns. Four linear potentiometers (LPs) were also applied to measure the specimen deformation under loading at the load application point and at the corbel ends (cantilever tips). The displacement used in the load \times displacement graphs reported in the results consisted of the displacement measured at the end of the corbel while subtracting the portion of the displacement measured at the point of application of load on the column in order to obtain only the vertical displacement of the corbel.

Regarding the materials' proportions, Wilson et al. [4] described the mix used for concrete, including the additions and additives, and highlighted the use of coarse aggregate of limestone origin (limestone) with a maximum diameter of 25 mm.

A series of cylindrical specimens (100 \times 200 mm) were cast to measure the mechanical properties of the concrete. The cylinders were tested following the respective ASTM standards [19–21] to determine the concrete compressive strength at 28 days ($f_{cm,28}$), compressive strength (f_{cm}), modulus of elasticity (E_c), and splitting tensile strength (or diametral compression strength ($f_{tm,sp}$)) at the time of testing of each specimen. The mechanical properties of the steel used in the primary reinforcement (ties) and secondary reinforcements were also measured using the ASTM code provisions [22], with f_{ym} and f_{ut} being the reinforcement yield strength and reinforcement ultimate strengths, respectively. Table 1 presents the average values measured for each property.

Table 1. Summary of measured mechanical properties of the concrete and reinforcing bars from Wilson et al. [4].

Proprieties (MPa)		Test Method	C0	C1	C2	C3
Concrete	$f_{cm,28}$ (MPa)	ASTM C39 [19]	31.72		44.82	
	f_{cm} (MPa)	ASTM C39 [19]	36.54	44.82	46.88	38.61
	E_c (MPa)	ASTM C469 [20]	33,784	43,436	44,816	34,474
	$f_{tm,sp}$ (MPa)	ASTM C496 [21]	3.79	4.21	4.41	4.55
φ 12.7 mm	f_{ym} (MPa)		478		463	
	f_{um} (MPa)		683		661	
φ 25.4 mm	f_{ym} (MPa)	ASTM A370 [22]	506		487	
	f_{um} (MPa)		701		685	
φ 28.58 mm	f_{ym} (MPa)		510		496	
	f_{um} (MPa)		741		729	

The corbels were tested in the inverted configuration of their typical operation in a structure, as shown in Figure 5. The load was applied through a hydraulic ram with a capacity of 3560 kN at a rate of 2.67 kN per second to simulate a quasi-static loading

protocol and avoid dynamic effects. Nevertheless, this loading protocol did not allow us to evaluate the post-peak stage of the load-deflection graphs. In the numerical models (Section 4), displacement-controlled loading was applied to track the load-deflection graph after the maximum capacity. In practice, differences between the loading using a load-controlled and displacement-controlled load are negligible in this case (two-dimensional, statically determined loads). Nevertheless, attention to this aspect should be given when the cracking pattern and load distribution change according to the loading protocol, such as in testing slab–column connections [23] and when the loading rate may introduce dynamic effects. The corbels were supported on one side by a roller support and on the other side by a hinged support through a metal plate measuring 203×356 mm. Load cells were installed on the supports to measure reaction forces.

For the C0 corbel, the center of the supports was placed at a distance of 368 mm from the face of the column, resulting in a ratio $a/d = 0.66$. For corbels C1, C2, and C3, a distance of 343 mm was used, resulting in corbels with a ratio $a/d = 0.59$. Test results will be presented together with numerical simulation results.

4. Proposed Modeling Approach

4.1. Overview and Boundary Conditions

The numerical modeling was carried out using Abaqus/CAE software version 6.14. Next, the parameters related to the modeling of corbel C2 were described in more detail. In the modeling of the corbels, two symmetry planes were considered, as sketched in Figure 6, by simulating only a quarter of the corbel. This approach had the main benefit of reducing the number of finite elements used in the model, thus ensuring a lower processing time for the simulation.

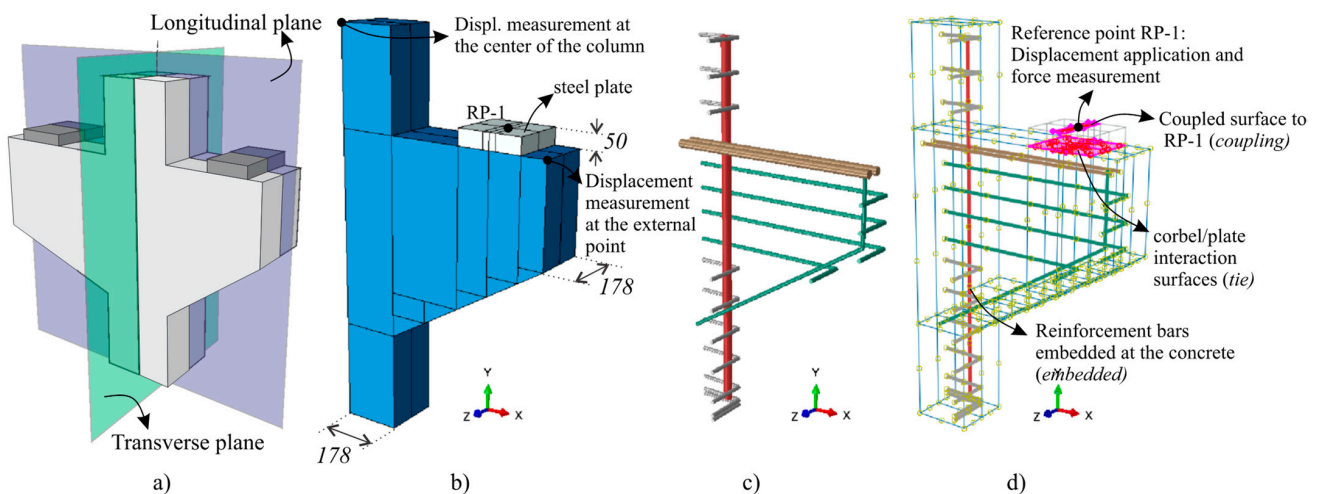


Figure 6. (a) Symmetry planes considered in the corbels; (b) geometry of the corbel and plate support; (c) reinforcement configuration; (d) interactions in the model.

Figure 6b shows the three-dimensional modeling of a quarter of the corbel tested by Wilson et al. [4] along with cuts in the geometry to assist the automatic mesh generation. Due to symmetry, the width of the corbel and column resulted in 178 mm. To avoid stress concentration at the point of load application, a steel plate with the same dimensions in the plane as the support of the experimental model was modeled, and because the thickness of the support was not informed, a value of 50 mm was adopted.

The reinforcement bars were modeled according to the geometry adopted by Wilson et al. [4] and the symmetry planes, resulting in two bars for tie reinforcement, one longitudinal bar for the column, and modeling only one-quarter of the stirrups and secondary reinforcement as shown in Figure 6c.

Figure 6d shows the reference point where the force was applied through the displacement control (RP-1). This point was coupled to the surface of the plate through the coupling

tool available in Abaqus, causing the degrees of freedom of the nodes of this surface to be connected with the point RP-1. This surface had the same width as the plate in the z -axis direction and a length of 40 mm in the x -axis direction. In addition, Figure 6d shows the plate's lower surface attached to the corbel's upper face using the tie interaction, where the nodes of the finite elements of both faces were connected. Finally, the reinforcements were embedded in the geometry of the corbel using an embedded tool while considering perfect adhesion and no sliding between the steel and the concrete. In general, this approach is a simplification that tends to increase the stiffness of the load-deflection response but does not significantly influence the governing failure mechanism and ultimate capacity of the numerical models. In practice, this occurs because the reinforcement sliding is limited when anchorage failure is not the governing failure mechanism of the tests.

The displacement in x and the rotations around the y -axis and z -axis were constrained in the YZ plane to apply the model symmetries, as shown in Figure 7a. In the XY plane, the displacement in z and the rotations in relation to x and y were constrained (Figure 7b). The displacements on the y -axis on its lower face were constrained to simulate the support at the base of the column, as shown in Figure 7c. As previously stated, the force was applied through displacement control at the RP-1 point, imposing a displacement of -6.5 mm in the y -direction.

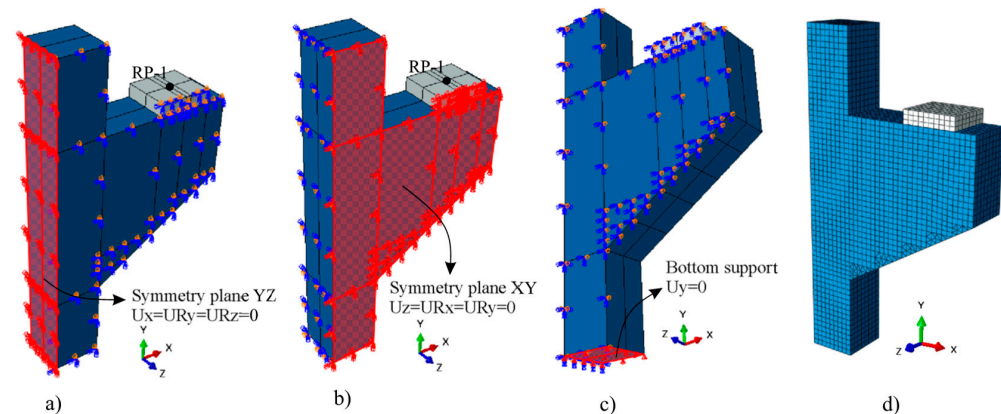


Figure 7. Boundary conditions: (a) symmetry in YZ ; (b) symmetry in XY ; (c) bottom support; (d) mesh discretization.

4.2. Concrete Modeling

The uniaxial stress–strain behavior of concrete in compression was considered, as illustrated in Figure 8a, and could be divided into three segments. The first segment was linear with a secant modulus of elasticity E_c up to the stress σ_{c0} , which was considered 40% of the ultimate stress (σ_{cu}) as recommended by the *fib* Model Code 2010 [24]. The second segment (hardening) was ascending and characterized by a non-linear behavior up to the ultimate stress (σ_{cu}) with the corresponding strain ε_{c1} . The ultimate stress ($\sigma_{cu} = f_{cm}$) adopted was the same measured by Wilson et al. [4], and the strain ε_{c1} was estimated by using the EN 1992-1-1:2004 expression [25] as shown in the expression (10).

$$\varepsilon_{c1} = \frac{0.7f_{cm}^{0.31}}{1000} \leq 0.0028 \quad (13)$$

The third segment (softening) was descending and non-linear and considered a residual stress of 5 MPa, as Syroka et al. [10] recommended to avoid numerical instability or convergence problems.

The hardening and softening segments (stages 2 and 3) were modeled according to Krätzig and Pölling [26]:

$$\text{Stage 2 in compression : } \sigma_c(\varepsilon_c) = f_{cm} \left[\frac{E_{ci}\varepsilon_c / f_{cm} - (\varepsilon_c / \varepsilon_{c1})^2}{1 + (E_{ci}\varepsilon_c / f_{cm} - 2)\varepsilon_c / \varepsilon_{c1}} \right] \quad (14)$$

$$\text{Stage 3 in compression : } \sigma_c(\epsilon_c) = \left(\frac{2 + \gamma_c f_{cm} \epsilon_{c1}}{2 f_{cm}} - \gamma_c \epsilon_c + \frac{\gamma_c \epsilon_c^2}{2 \epsilon_{c1}} \right)^{-1} \quad (15)$$

$$\gamma_c = \frac{\pi^2 f_{cm} \epsilon_{c1}}{2 \left[\frac{G_{ch}}{l_d} - 0.5 f_{cm} \left(\epsilon_{cm} (1 - b) + b \frac{f_{cm}}{E_c} \right) \right]^2} \quad (16)$$

The value of $b_c = 0.7$ was assumed in the calculations. The crushing energy G_{ch} was calculated according to Oller [27]:

$$G_{ch} = \left(\frac{f_{cm}}{f_{tm}} \right) \cdot G_f \quad (17)$$

The stress–strain behavior in tension was modeled according to Hordijk [28] (Figure 8b):

$$\sigma_t(w) = f_{tm} \left\{ \left[1 + \left(c_1 \frac{w}{w_c} \right)^3 \right] e^{-c_2 \frac{w}{w_c}} - \frac{w}{w_c} (1 + c_1^3) e^{-c_2} \right\} \quad (18)$$

with : $c_1 = 3; c_2 = 6.93; w_c = 5.14 G_f / f_{tm}$

Therefore, the tensile behavior was grounded in stress–crack-opening relationships, the fracture energy G_f , and the finite element size l_{eq} . The fracture energy G_f was determined according to *fib* Model Code 1990 expressions [29]. The stress–crack-opening relationship $\sigma_t \times w$ was transformed to the stress–strain behavior $\sigma_t \times \epsilon_t$ using the same approach from Genikomsou and Polak [11] (Figure 8c).

$$\epsilon_t = \epsilon_{tu} + w / l_d \quad (19)$$

The damage evolution parameters in compression and tension were determined according to the simplified expressions presented by Yu et al. [30].

Some of the parameters that defined the yield surface and plastic flow rule in CDP were determined based on a calibration study, and others were determined using experimentally based values from the literature. The following parameter values were used: eccentricity of the potential plastic surface, $e = 0.1$ [15]; dilatancy angle, $\psi = 42$ (calibrated); the ratio between the biaxial and uniaxial compressive strengths, $\sigma_{b0} / \sigma_{c0} = 1.16$ [31,32]; the ratio of second stress invariants on the tensile and compressive meridians, $K_c = 0.667$ [15,33]; and the viscosity parameter μ , between 0 and 10^{-5} . The finite element size varied between 20 mm and 25 mm between different numerical models. Nevertheless, a specific mesh study was performed to support this choice that will be shown in the following sections.

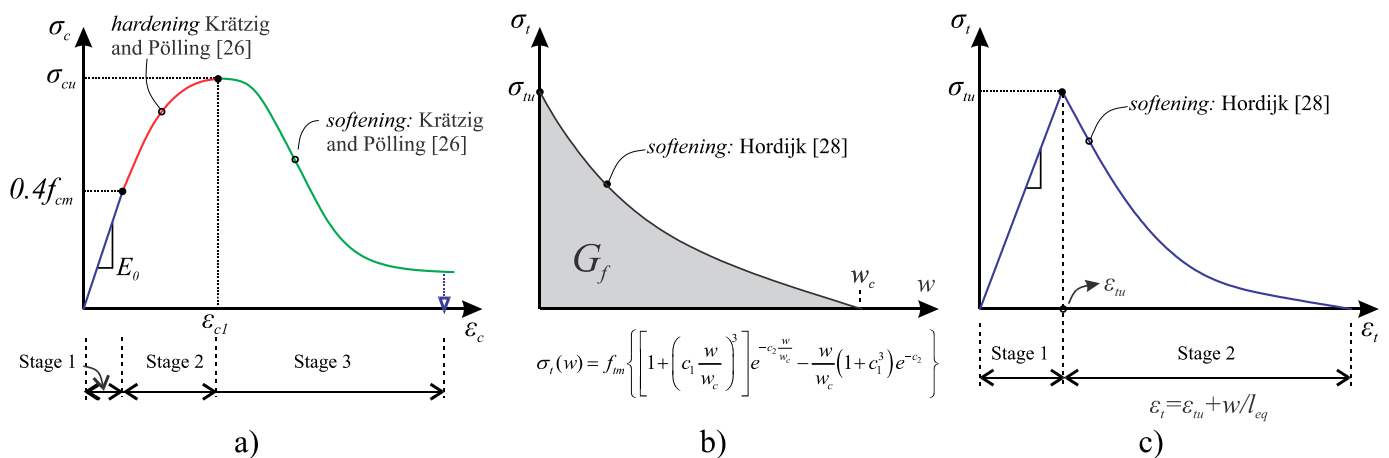


Figure 8. (a) Uniaxial compressive stress–strain behavior for concrete [26]; (b) uniaxial tensile stress–crack-width relationship [28]; (c) uniaxial tensile stress–strain relationship.

4.3. Reinforcement Material Model

The constitutive model adopted for steel bars was the simplified model from the *fib* Model Code 2010 [24], for which an elastoplastic model with linear hardening was assumed. A class A steel with an f_u/f_y ratio of 1.1, ultimate strain ($\epsilon_{s,u}$) of 2.5%, and modulus of elasticity (E_s) of 200 GPa was adopted. In simulations performed with and without the hardening stage, the results were similar (even when failure was governed by the primary reinforcement yielding) due to the slight hardening adopted in this model. Despite this small influence, a slight hardening was advantageous, as it avoided numerical issues associated with zero stiffness in numerical model processing [34].

4.4. Mesh

The geometry of the corbels and the steel plate were meshed with three-dimensional solid finite elements. For the corbels, the finite elements C3D8 (solid with six faces) and C3D6 (solid with five faces in the shape of a triangular prism or wedge) were used; for the steel plate, only the element C3D8 was applied. Elements C3D8 and C3D6 consisted of three-dimensional elements with eight and six nodes, respectively, and three degrees of freedom of translation per node, resulting in elements with a linear approximation for displacements. The C3D8 element was used in almost all of the corbels. After a mesh sensitivity study, the average element size chosen was $l_{eq} = 20$ mm.

The reinforcements were meshed with one-dimensional truss finite elements with two nodes using a linear approximation of the displacements. For the reinforcement of the column and the constructive reinforcement of the corbels, the truss finite element T3D2 was adopted, in which each node had three translational degrees of freedom. As for the primary and secondary reinforcements, the beam element B31 was adopted, in which each node had six degrees of freedom (three for translation and three for rotation).

4.5. Solution Procedure and Load Application

The simulations were performed using the ABAQUS/Standard package [15], in which the Newton–Raphson algorithm was applied as the solution procedure. The automatic increment size definition from ABAQUS was applied, which allowed for a decrease in the processing time when convergence was achieved smoothly. Similar to other studies, the load and boundary conditions were applied in different steps [35]: (i) in the first step, only the boundary conditions were applied; and (ii) in the second step, the vertical displacement was applied at the loading plate (Figure 6d). Unlike what is commonly applied in steel structures [35], the initial geometry defects were not considered in the simulations.

5. Validation of the Modeling Approach

Figures 9–12 shows the comparison between the experimental results reported by Wilson et al. [4] and the numerical results using the proposed modeling approach for corbels C0, C1, C2, and C3, respectively.

Part (a) of each figure shows the load \times displacement behavior of the tests and numerical models, in which the following aspects can be highlighted: (i) the load corresponding to the first observation of cracks in the corbel; (ii) the point at which the reinforcing bars started to yield in one or more bars of the tie (primary reinforcement); (iii) the point where all the tie bars had yielded; and (iv) the point where the corbel reached the ultimate load (peak value). In the numerical models, notably, the interval between the yield point of the first reinforcement and the yield point of all reinforcements in the tie was much smaller when compared to the experimentally tested corbels. This behavior occurred due to the ideal loading conditions (perfect symmetry) and homogeneous material property distribution assumed in the numerical models, which in practice are not fully true in real structures.

Part (b) of Figures 9–12 shows a 3D perspective view of the corbel, illustrating the reinforcement bars and the isovalue surface of the maximum plastic deformations at the instant of ultimate load. In practice, this view illustrates the inner cracking pattern at the corbels. Part (c) of Figures 9–12 corresponds to the maximum plastic deformations on the

outer face of the corbel and part (d) to the tensile damage d_t (also at the instant of ultimate load). In general, there was a close correlation between the regions of maximum plastic strains and tensile damage. Part (e) of Figures 9–12 shows the cracking pattern of the corbel tested after failure along with information on the cracking pattern evolution.

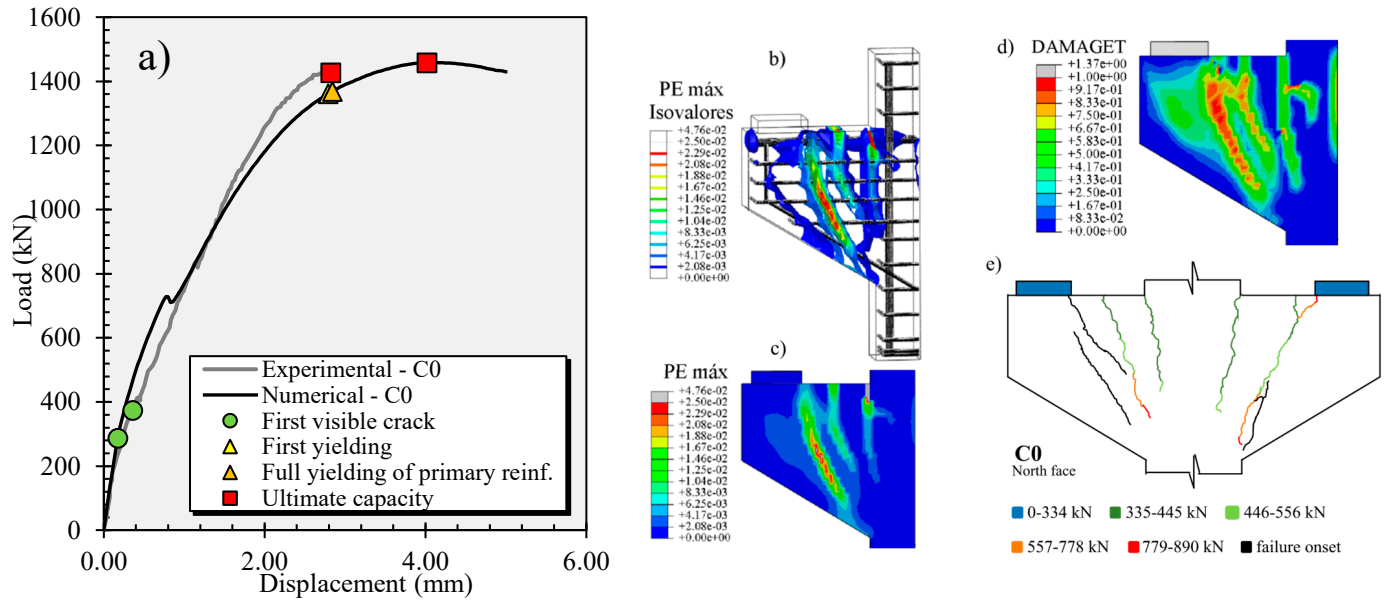


Figure 9. Comparison between experimental and numerical results for corbel C0: (a) load-deflection response; (b) sketch of the distribution of inner cracking in the numerical model through isovalues of plastic strains; (c) distribution of maximum plastic strains; (d) distribution of tensile damage in the corbel and (e) in the experiment (north face).

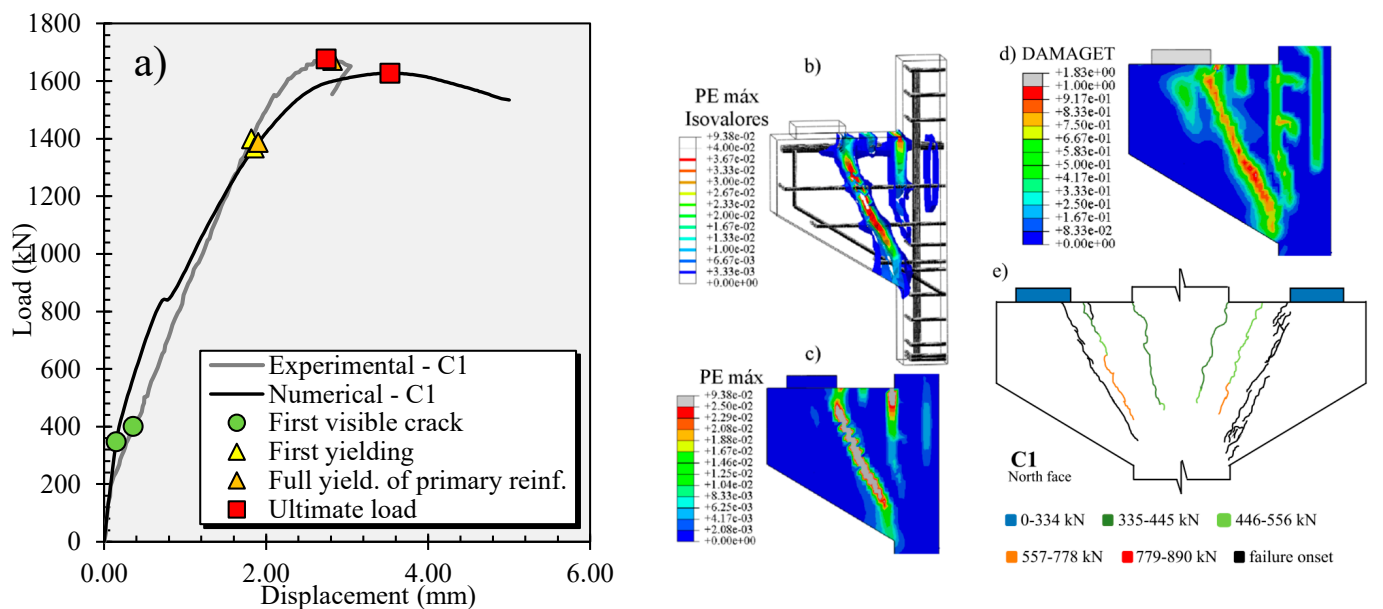


Figure 10. Comparison between experimental and numerical results for corbel C1: (a) load-deflection response; (b) sketch of the distribution of inner cracking in the numerical model through isovalues of plastic strains; (c) distribution of maximum plastic strains; (d) distribution of tensile damage in the corbel and (e) in the experiment (north face).

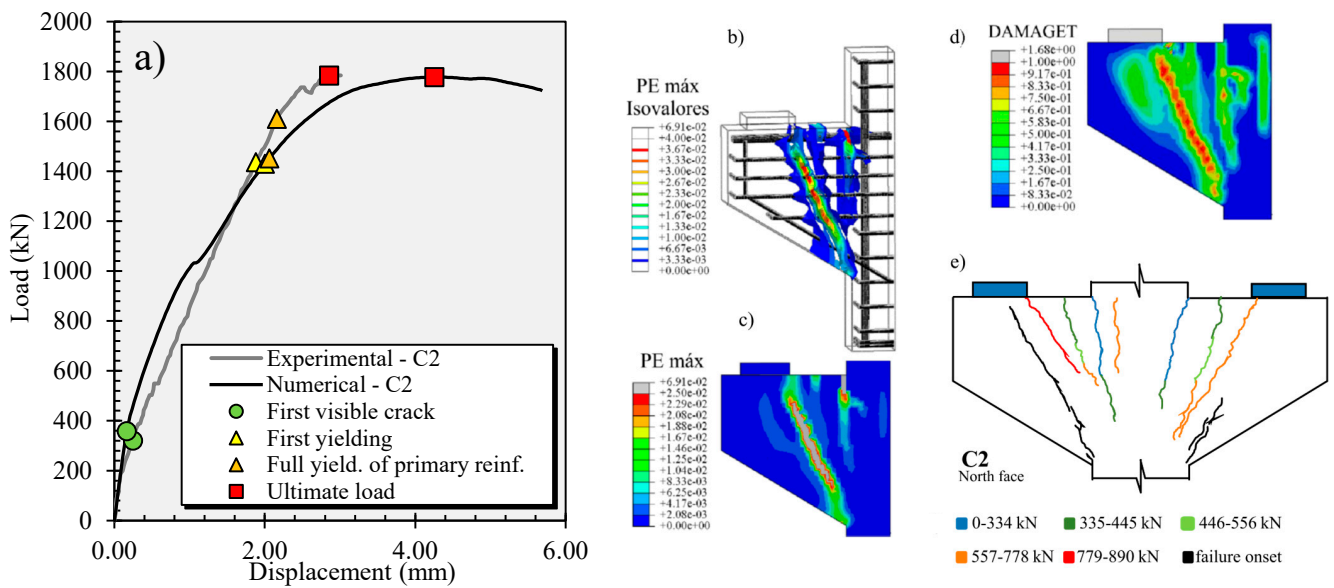


Figure 11. Comparison between experimental and numerical results for corbel C2: (a) load-deflection response; (b) sketch of the distribution of inner cracking in the numerical model through isovalues of plastic strains; (c) distribution of maximum plastic strains; (d) distribution of tensile damage in the corbel and (e) in the experiment (north face).

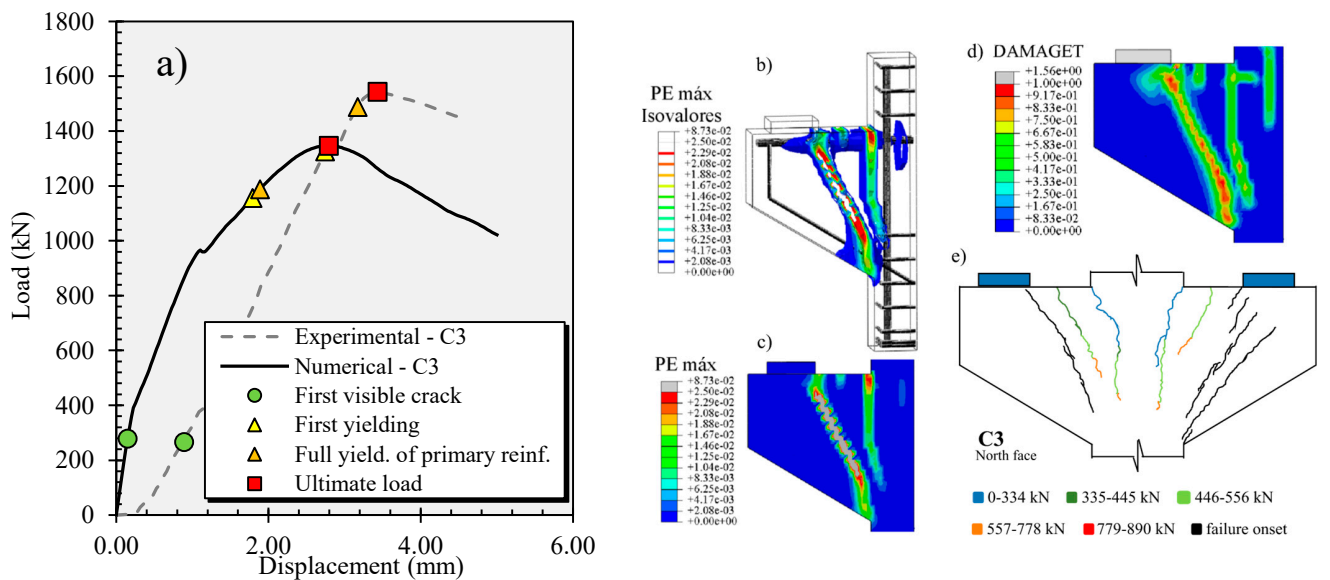


Figure 12. Comparison between experimental and numerical results for corbel C3: (a) load-deflection response; (b) sketch of the distribution of inner cracking in the numerical model through isovalues of plastic strains; (c) distribution of maximum plastic strains; (d) distribution of tensile damage in the corbel and (e) in the experiment (north face).

5.1. Load × Displacement Graphs

The first linear stage characterized the load × displacement graphs of the numerical models. Next, after the development of concrete plastic strains (cracking) in the upper region between the corbel and the column, the slope of the load-deflection graph decreased until the beginning of the cracks in the region of the strut. At this point, a new change in the slope of the graph occurred, and the specimen failed with a gradual stiffness decrease. In general, the numerical model graphs were mostly similar to the experimental ones. The main difference between the experimental and numerical graphs was the higher stiffness of the numerical curves compared to the experimental ones, a typical characteristic in studies

using CDP [11,36]. In general, these differences can be related mainly to not considering support accommodations during the loading and also to considering the perfect bond between the concrete and the reinforcement. In corbel C3 (in which the experimental and numerical graphs deviated more), the linear potentiometer that measured the displacements in the support region presented a malfunction, according to Wilson et al. [4]. Thus, the displacement of the experimental curve of the corbel C3 represented the displacement of the corbel end by adding the deformations arising from the support points.

5.2. Cracking Pattern

Regarding the cracking pattern, the experiments and numerical models provided similar results.

Both cracks started in the upper region between the corbel and the column under similar loads (green dots in the load \times displacement graphs); With the load increase, a second crack arose between the column and the support plate. This crack was relatively smaller in numerical models of corbels C1, C2, and C3. In the C0 corbel, the extension of this crack was more similar to that observed in the experiment.

With the load increase, the third crack appeared in the central region of the strut. Note that on the south face of corbel C0, the crack appeared between loads of 779 and 890 kN, which was the range in which the drop in stiffness appeared in the load \times displacement plot of the numerical model. In the experimental corbel C2, the crack appeared between loads of 557 and 778 kN, while in the numerical model, the crack began to appear at a higher load of around 950 kN.

Finally, the failure of the corbels was characterized by a brittle mechanism similar to shear and punching shear failures [37–40] and triggered by the propagation of the third crack, which started in the lateral region of the support plate and extended to the inferior region close to the column (crossing the strut region). According to Wilson et al. [4], corbels C0 and C2, which presented higher ratios of secondary reinforcement, had smaller crack openings than the others, which agreed with the lower values of plastic strains in the simulations of these corbels at failure.

5.3. Stresses in the Reinforcing Bars

Wilson et al. [4] explained that all tested corbels presented primary reinforcement yielding at the failure onset except for corbel C0. It can be observed in the load \times displacement plot that for corbels C1 and C2, the beginning of the reinforcement yielding in the numerical model matched the beginning of the reinforcement yielding in the test. For corbel C3, the beginning of the reinforcement yielding in the numerical model occurred at a load level 12.8% lower than the experimental one. Nevertheless, in both cases, the reinforcement-yielding loads corresponded to approximately 85% of the respective failure loads. According to reference [4], the primary reinforcement (tie) tensile stress for corbel C0 was between 455 and 483 MPa at failure. This stress level corresponded to between 90% and 95% of the reinforcement yield strength, showing that this reinforcement was on the verge of yielding at the failure. In the numerical model of C0, the primary reinforcement (tie) showed a small reinforcement yield before failure that started at a load level of 1368.5 kN, corresponding to 94% of the failure load.

Table 2 presents the ultimate capacity achieved in the experiments (F_{EXP}) and in the finite element models (F_{FEM}). In general, the finite element models closely predicted the ultimate capacities for the C0, C1, and C2 corbels, with a maximum difference of 3.01%. The larger deviation occurred for the simulation of the corbel C3, which presented an ultimate load of 12.77% below the experimental one. The average ratio between the tested and predicted resistances was 0.97 with a coefficient of variation equal to 6.79%. Therefore, the level of accuracy was considered satisfactory compared to that in other publications related to the NLFEM of corbels using different constitutive models [5,6].

Table 2. Comparison between experimental and predicted ultimate loads with the FEM.

Corbel	F_{EXP} (kN)	F_{FEM} (kN)	F_{FEM}/F_{EXP}	Error
C0	1426.23	1458.01	1.02	2.22%
C1	1677.65	1627.23	0.97	3.01%
C2	1784.45	1778.17	1.00	0.35%
C3	1544.15	1346.93	0.87	12.77%
		AVG	0.97	
		COV (%)	6.79%	

6. Sensibility Study

6.1. Stress–Strain Behavior in Tensile

Figure 13 shows different stress–strain behavior models in tension. In this case, the fracture energy G_f was determined according to the *fib* Model Code 1990 [29]. It was observed that the models by Genikomsou and Polak [11] and the *fib* Model Code 2010 [24] were bilinear, and those by Hordijk [28] and Guo [41] were exponential. The models from the *fib* Model Code 2010 [24], Genikomsou and Polak [11], and Hordijk [28] are based on the concept of fracture energy and showed similar plots. Nevertheless, Guo’s model [41], with α_t calculated according to the author’s formulation ($\alpha_{t,calc} = 4.92$), resulted in a sharp drop in the softening stage compared to the other models. For illustration purposes, using $\alpha_t = 0.3$, the softening stage decreased more smoothly, resulting in higher residual tensile stresses.

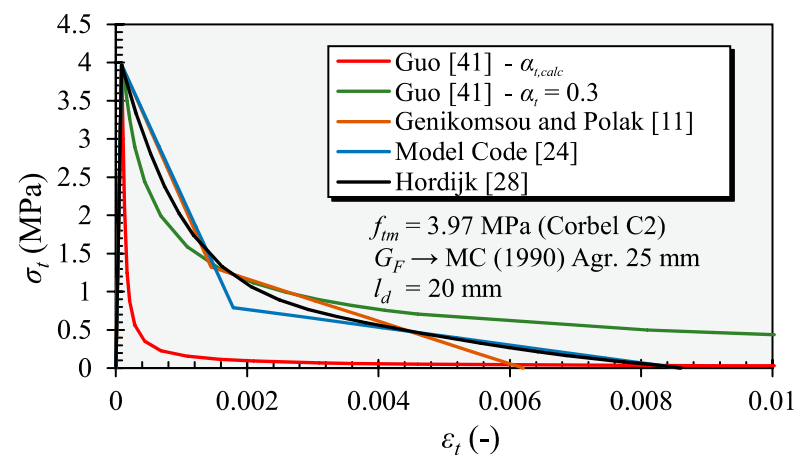


Figure 13. Stress–strain behavior in tension according to different analytical models using data from corbel C2 [11,24,28,29,41].

Figure 14 shows the effects of different stress–strain behavior models in tension on the numerical results regarding the load \times displacement response and cracking pattern. The results from Guo’s [41] model with $\alpha_{t,calc} = 4.92$ are not presented due to the convergence issues caused by the sudden drop in the residual tensile strength (softening stage), which aborted the processing even at the beginning of the analysis. Herein, the results presented for the Guo models are the ones with the manually altered value of $\alpha_t = 0.3$. Regarding the load \times displacement plots, all the tested models presented a similar behavior until the ultimate load; after the peak, the bilinear models presented a more accentuated drop when compared to the exponential ones. In general, the similar peak loads achieved could be expected since the residual tensile strength was similar for all tested models (see Figure 15). Nevertheless, when using higher values of α_t , it is expected that a more significant difference would appear in the simulations.

Regarding the cracking pattern indicated by the maximum plastic strains, the models based on the concept of fracture energy showed similar patterns throughout the analysis (Figure 14a–c). These models began to develop tensile plastic strains (cracking) at the interface between the corbel and the column, and with the load increase, an inclined main

plastification appeared in the central region of the strut. When using the model by Guo [41], nevertheless, the behavior differed through the development of two main cracks within the strut zone with smaller values of plastic strains.

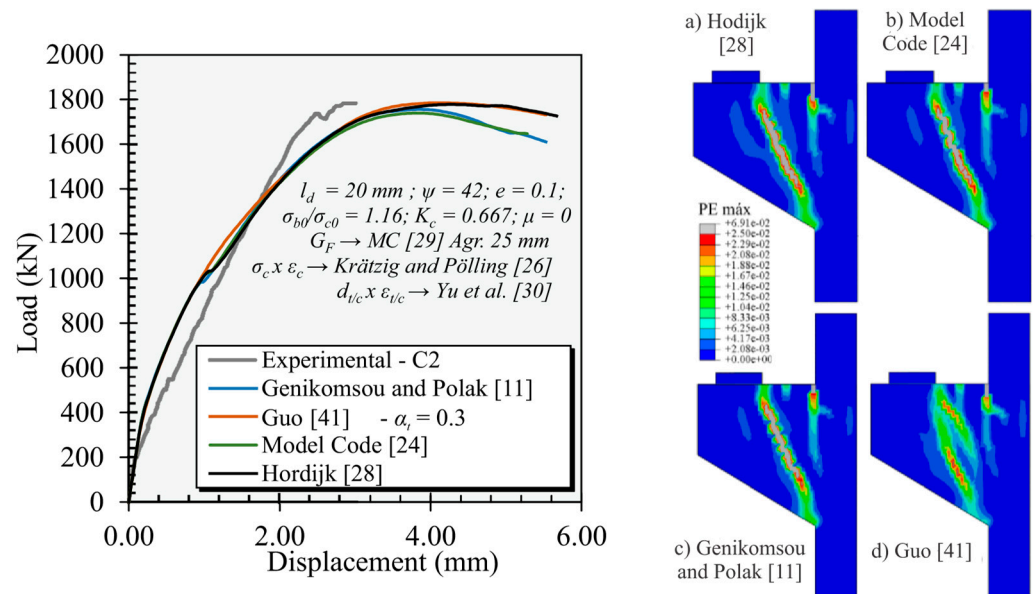


Figure 14. Effects of different stress–strain behavior models in tension on the load \times displacement response and cracking pattern of the FEM of corbel C2 [11,24,26,28–30,41].

The use of models based on the concept of fracture energy is widely employed in numerical simulations found in the literature [11,12,36,42–44] because it decreases the mesh dependence of the results [12]. In fact, in tests performed with Guo’s model [41] that varied the mesh discretizations, the numerical results presented larger changes. Therefore, the tensile stress–strain behavior model of concrete in tension was modeled according to Hordijk [28] in the next analyses.

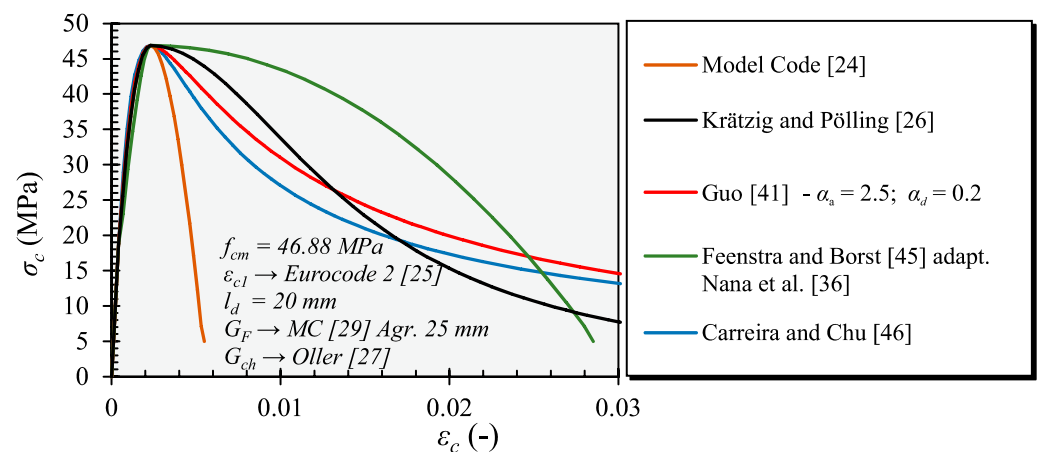


Figure 15. Stress–strain behavior in compression according to different analytical models using data from corbel C2 [24–27,29,36,41,45,46].

6.2. Stress–Strain Behavior in Compression

Figure 15 illustrates the five models presented to describe the stress–strain behavior in compression using the concrete properties of corbel C2 [24,26,41,45,46]. In general, the plots of the models differed only slightly in the second section (the hardening branch). On the other hand, the models showed significantly different results in the third stretch (the softening stage). The *fib* Model Code 2010 formulation [24] provided a parabolic

behavior that caused the curve to fall more sharply when compared to the other models. The formulations by Feenstra and Borst [45] and Krätzig and Pölling [26] presented higher residual compressive strength due to considering the finite element size l_d and crushing energy concepts in the expressions. For Guo’s [41] model, the parameters $\alpha_d = 2.5$ and $\alpha_d = 0.2$ were used for comparison.

Figure 16 shows the effect of different stress–strain behavior models in compression on the load \times displacement response and cracking pattern of the FEM of corbel C2. Regarding the load \times displacement response, similar results were observed up to a load of 1500 kN. After this loading stage, larger differences between the models could be observed. Using the fib Model Code 2010 expressions [24], the corbel failed at a load level well below the experimental in a brittle way. The other tested models resulted in higher resistance capacity with a more ductile failure mechanism. Regarding the cracking pattern, all models showed plastic strains in similar regions, starting with the deformations at the interface between the corbel and the column and a main crack in the central region of the strut. Figure 16c shows that the model by Feenstra and Borst [45] presented larger tensile plastic strains when compared to the fib Model Code model 2010 [24].

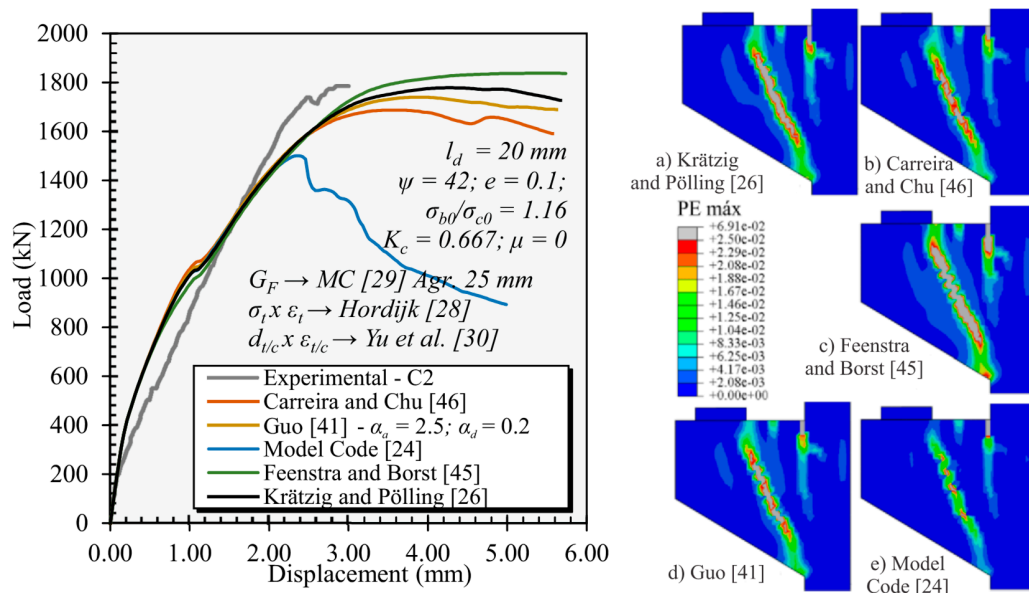


Figure 16. Effect of different stress–strain behavior models in compression on the load \times displacement response and cracking pattern of the FEM of corbel C2 [24,26,28–30,41,45,46].

The differences in the numerical results and cracking patterns were directly related to the third section of each analytical model used. In other words, the lower rate of residual strength decrease in the constitutive model tended to increase the ultimate capacity of the corbels since it hampered premature compression failures at the nodes and struts. In the same way, analytical models with a higher residual compressive strength (larger area below the curve in the softening stage) tended to increase the deformation capacity (ductility) at failure.

6.3. Damage Evolution Laws

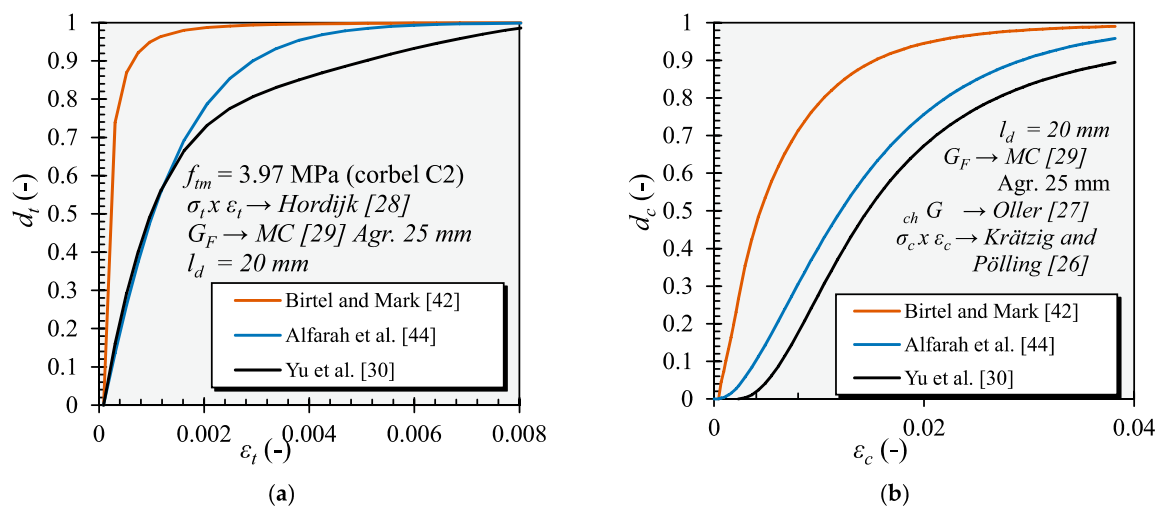
As previously explained, the scalar damage parameters in tension (d_t) and compression (d_c) acted on decreasing the elastic modulus E in the stress–strain graphs and varied from 0 to 1 (0 when the material was intact and 1 when the material was fully damaged). In CDP, the damage variables were inputted through the inelastic strains \times damage relationship ($\epsilon_c^{in} \times d_c$ and $\epsilon_t^{in} \times d_t$). The evolution of the scalar damage variables according to the inelastic strain could be determined according to different models (Table 3).

Table 3. Analytical models to describe the evolution of tensile and compressive damage parameters.

Reference	Damage Evolution Models	
	Tensile	Compressive
Birtel and Mark [42]	$d_t = 1 - \frac{\sigma_t E_c^{-1}}{\varepsilon_t^{pl} (1/b_t - 1) + \sigma_t E_c^{-1}}$ with: $\varepsilon_t^{pl} = b_t \varepsilon_t^{in}$; $b_t = 0.1$	$d_c = 1 - \frac{\sigma_c E_c^{-1}}{\varepsilon_c^{pl} (1/b_c - 1) + \sigma_c E_c^{-1}}$ with: $\varepsilon_c^{pl} = b_c \varepsilon_c^{in}$; $b_c = 0.7$
Yu et al. [30]	$d_t = 1 - \frac{\sigma_t}{f_{tm}} \text{ for } \varepsilon_t \geq \varepsilon_{tu}$	$d_c = 1 - \frac{\sigma_c}{f_{cm}} \text{ for } \varepsilon_c \geq \varepsilon_{c1}$
Alfarah et al. [44]	$d_t = 1 - [2(1 + a_t) \exp(-b_t \varepsilon_t^{in}) - a_t \exp(-2b_t \varepsilon_t^{in})] / (2 + a_t)$ With: $b_t = \frac{\sigma_{c0} l_d}{G_F} (1 + \frac{a_t}{2})$; $a_t = 2 \left(\frac{f_{tm}}{\sigma_{t0}} \right) - 1 + 2 \sqrt{\left(\frac{f_{tm}}{\sigma_{t0}} \right)^2 - \left(\frac{f_{tm}}{\sigma_{t0}} \right)}$	$d_c = 1 - [2(1 + a_c) \exp(-b_c \varepsilon_c^{in}) - a_c \exp(-2b_c \varepsilon_c^{in})] / (2 + a_c)$ With: $b_c = \frac{\sigma_{c0} l_d}{G_{ch}} (1 + \frac{a_c}{2})$; $a_c = 2 \left(\frac{f_{cm}}{\sigma_{c0}} \right) - 1 + 2 \sqrt{\left(\frac{f_{cm}}{\sigma_{c0}} \right)^2 - \left(\frac{f_{cm}}{\sigma_{c0}} \right)}$

As shown in Table 3, the model by Yu et al. [30] is a simpler formulation in which the damage is considered only in the softening stage (after reaching the peak compressive and tensile strengths). The models by Birtel and Mark [42] and Alfarah et al. [44] consider the damage evolution after the elastic stage and are experimentally calibrated models; the model by Alfarah et al. [44] is the most refined one as it takes into account the fracture and crushing energies and the size of the finite element.

Figure 17 shows the damage evolution according to different models presented in Table 3. In general, the model by Birtel and Mark [42] damaged the material at a faster rate, both in tension and compression, when compared to the other two models. For tensile damage (Figure 17a), the models by Yu et al. [30] and Alfarah et al. [44] had a similar evolution up to a $d_t = 0.6$, and after this, the model by Alfarah et al. [44] showed larger damage values. It is noteworthy here that as the tensile behavior of concrete was considered linear until failure, σ_{t0} in the expressions by Alfarah et al. [44] was assumed to be equal to f_{tm} (thus, $a_t = 1.0$). In compression, these two damage models showed similar damage evolution rates, differing only in the damage onset point.

**Figure 17.** Comparison of the different damage evolution models in (a) tension [28–30,42,44] and (b) compression [26,27,29,30,42,44] ($f_{cm} = 46,88$ MPa; $\varepsilon_{c1} \rightarrow$ calculated based on [25]).

Despite the elastic modulus degradation having a clear impact on the simulations of cyclic tests, its influence on the results of static tests is unclear [11]. In practice, damage occurs both in static and cyclic tests because it is a physical characteristic of concrete after cracking. In addition, considering the damage parameters changes the proportion between the inelastic and plastic concrete strains (Section 2.1). Therefore, it could influence the numerical results due to changes in the magnitude of plastic strains. Lastly, the

redistribution of stresses and forces occurs in numerical models (even in static tests [47,48]) in a way in which the consideration of damage parameters could better simulate load relief in some regions in static tests. Because of this, some tests were conducted to investigate the influence of including or not including the damage parameters in the simulations of the corbels.

Some convergence issues appeared in the attempt to simulate corbels using the tensile damage evolution models by Birtel and Mark [42] and Alfarah et al. [44]. Using the model by Birtel and Mark [42], some simulations aborted shortly after the linear stage of the load × displacement graph (when the first flexural cracks arose). On the other hand, the simulations were aborted in the model by Alfarah et al. [44] before reaching the peak load. This occurred because these tensile damage models decreased the elastic modulus faster, hampering the numerical convergence. At this point, this problem occurred even when using higher values of viscoplastic regularization (μ values). Based on this, the model by Yu et al. [30] was chosen to be used in the reference modeling approach.

Figure 18 shows the FEM response of corbel C2 when varying only the compressive damage evolution models (the same model by Yu et al. [30] was used to describe the concrete tensile damage evolution). The load × deformation response using the model by Birtel and Mark [42] resulted in the lower predicted ultimate load (73% of the experimental one). The other two models provided similar predictions, diverging only when close to failure. In the end, the model by Alfarah et al. [44] resulted in a lower predicted capacity than when using the model by Yu et al. [30]. Therefore, models with higher damage evolution rates in compression (see Figure 17b) resulted in lower ultimate capacities of the corbel.

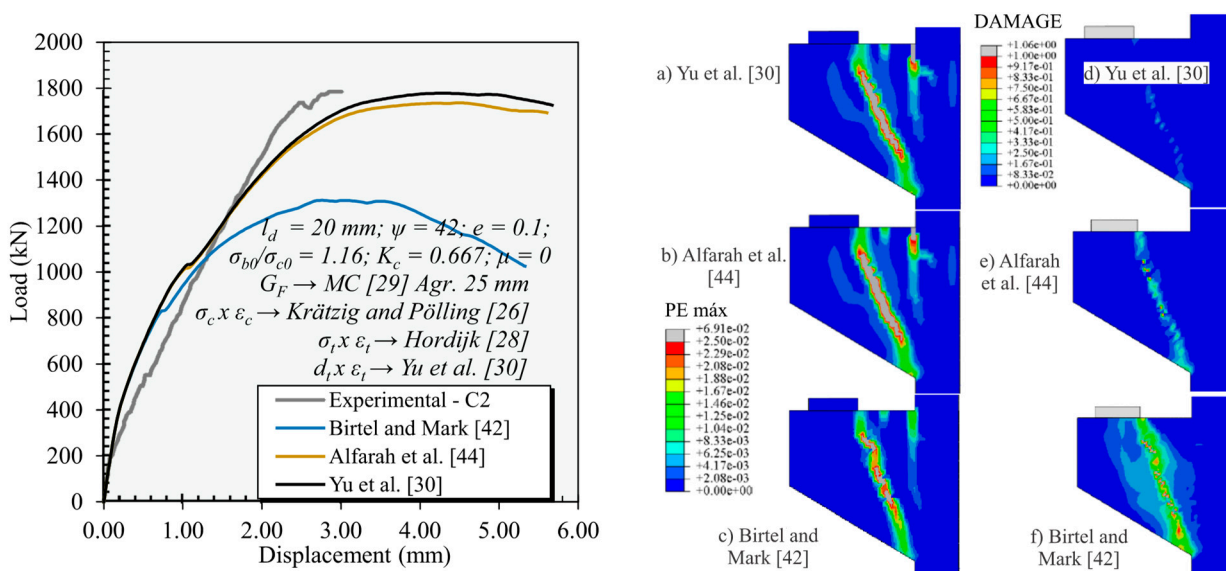


Figure 18. Effects of different compressive damage evolution laws on the load × displacement response and cracking pattern of the FEM of corbel C2 in terms of (a–c) maximum plastic strains and (d–f) compressive damage d_c [26,28–30,42,44].

Regarding the cracking pattern (see Figure 18a–c), the simulations using the models by Alfarah et al. [44] and Yu et al. [30] presented similar patterns. Nevertheless, the simulation using the model by Birtel and Mark [42] in compression showed lower plastic strains at the interface between the corbel and the column (lower crack openings), suggesting that the failure was triggered by the larger damage in the strut region, as confirmed in Figure 18d–f. Clearly, the compression strut was more damaged when using the model by Birtel and Mark [42] when compared to the other models.

Without including the damage parameters in the numerical analysis, the CDP model behaved just like a plastic model; that is, the plastic and inelastic strains became equal ($\epsilon^{pl} = \epsilon^{in}$). Figure 19 shows the numerical response of the corbel C2 with and without the

damage parameters (both in tension and in compression) to examine the effects that the damage parameters caused in the numerical results of the static tests.

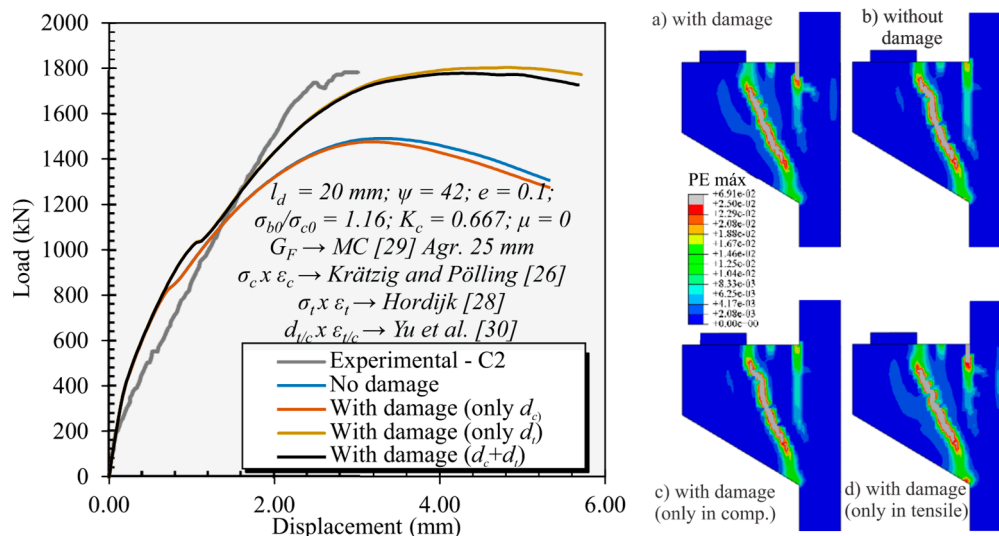


Figure 19. Load × displacement behavior and cracking pattern considering and not considering the damage parameters in the FEM of corbel C2 [26,28–30].

Figure 19 shows that damage parameters began to influence the numerical response at a load of 800 kN due to the concrete in some regions of the corbel remaining at the elastic stage and showing little or no damage. When damage parameters were applied only in compression (d_c), a similar response to that in the previous analysis was observed; that is, the damage increased at the strut region, resulting in a lower ultimate capacity of the numerical models. When only tensile damage (d_t) was considered, an increase in stiffness and ultimate load of the corbel was observed, as identified by Genikomsou and Polak [11] for slab–column connections failing in punching. Finally, when the tensile (d_t) and compressive (d_c) damage models were considered in the FEM, a combination of results was observed. In other words, an increase in stiffness due to d_t and a decrease in ultimate capacity due to d_c took place.

6.4. Yield Criterion Parameters— σ_{b0}/σ_{c0} and K_c

The parameter σ_{b0}/σ_{c0} , as previously explained, is the ratio between the equibiaxial and uniaxial compressive yield stress of concrete in compression. Experimental values of this parameter range from 1.10 to 1.16 [13], with 1.16 as the default value in ABAQUS.

Figure 20 shows the influence of varying the parameter σ_{b0}/σ_{c0} from 1.0 to 1.2 in the numerical results for corbel C2. In practice, the load × displacement graphs were quite similar up to a load of 1400 kN. Increasing the ratio σ_{b0}/σ_{c0} increased the ultimate capacity of the corbel slightly. In practice, no significant differences could be identified regarding the cracking pattern varying this parameter.

The K_c parameter determines the shape of the yield surface in the deviatoric stress plane under a triaxial stress state and must assume values between 0.5 and 1.0. According to Lubliner et al. [13], this parameter can be assumed as constant, and values from 0.64 to 0.8 can be observed experimentally. The value used by Lubliner et al. [13] and applied as the default in Abaqus© is 0.667.

Figure 21 shows the influence of the K_c value on the numerical response of corbel C2. In general, a similar load × displacement behavior was observed up to a load of 1250 kN for all curves. Nevertheless, with the increase in the load, lower values of K_c resulted in higher ultimate loads. Regarding the cracking pattern, higher values of K_c resulted in a higher concentration of tensile plastic deformations in the bottom region of the strut (nodal zone). This may explain the lower ultimate capacities of the corbels when K_c was increased.

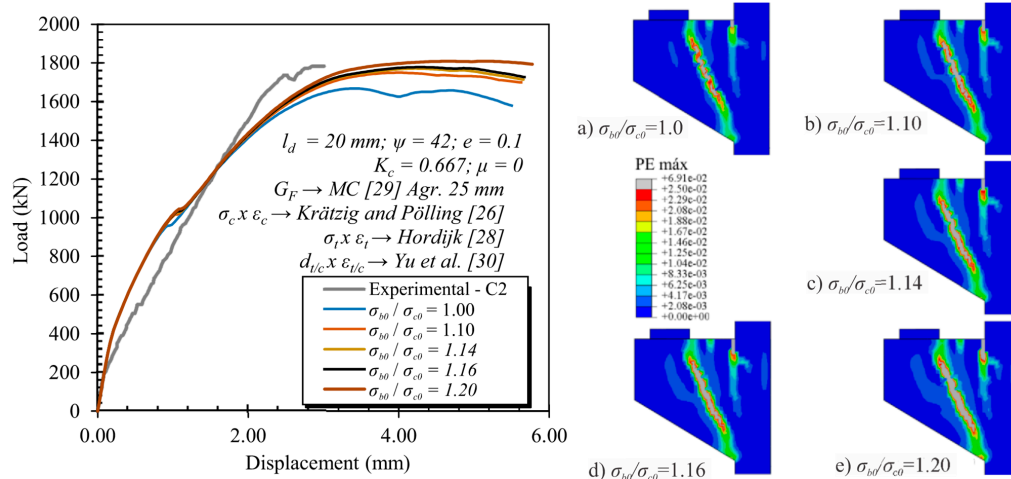


Figure 20. Influence of parameter σ_{b0}/σ_{c0} on load \times displacement behavior and cracking pattern of corbel C2 [26,28–30].

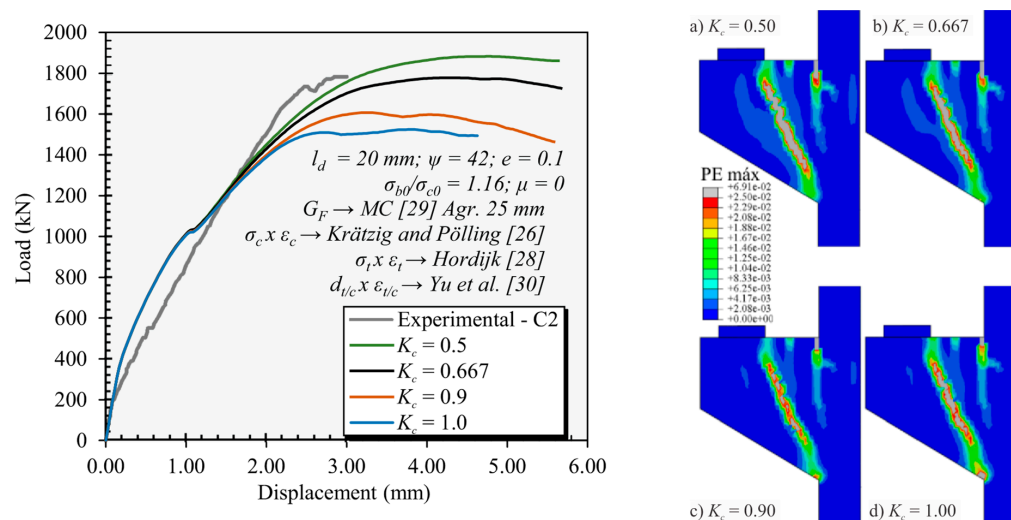


Figure 21. Influence of the K_c parameter on the load \times displacement behavior and cracking pattern of the FEM results for corbel C2 [26,28–30].

6.5. Plastic Flow Rule Parameters— e and ψ

The parameter e (eccentricity) defines the rate at which the potential function G (Drucker–Prager hyperbolic form) approaches the asymptote. By default, $e = 0.1$ is frequently adopted. If $e = 0$, the plastic potential would tend to be a straight line at the meridional plane (place p - q).

Figure 22 shows the influence of varying the eccentricity from 0.05 to 0.2 in the numerical results for corbel C2. In general, Figure 22 demonstrates that this parameter had a negligible influence on the global behavior of the corbel (load \times displacement graphs and on the cracking pattern). In practice, only a small increase in ultimate capacity was observed as the eccentricity value increased.

The dilation angle (ψ) is the angle measured in the p - q plane at high confinement pressures (triaxial tests), as explained earlier. In CDP, this angle must assume a value greater than zero and less than $\arctg(3/2)$; that is, $0^\circ < \psi < 56.31^\circ$. The Abaqus software does not provide any standard value for this parameter, which must be calibrated according to the concrete used in the absence of experimental results of triaxial tests.

A widely used approach used to calibrate the dilation angle is to simulate the tested specimens with varied values of dilation angle and when comparing the tested and predicted results, choose the value that best fits the experimental curve, as conducted in

Genikomsou and Polak [11] (the value ranged between 30° and 42°), Earij et al. [49] (the value varied between 20° and 50°), and Nana et al. [36] (the value varied between 30° and 45°). Nevertheless, smaller values between 13° and 15° are also commonly found in the literature, such as in Alfarah et al. [44].

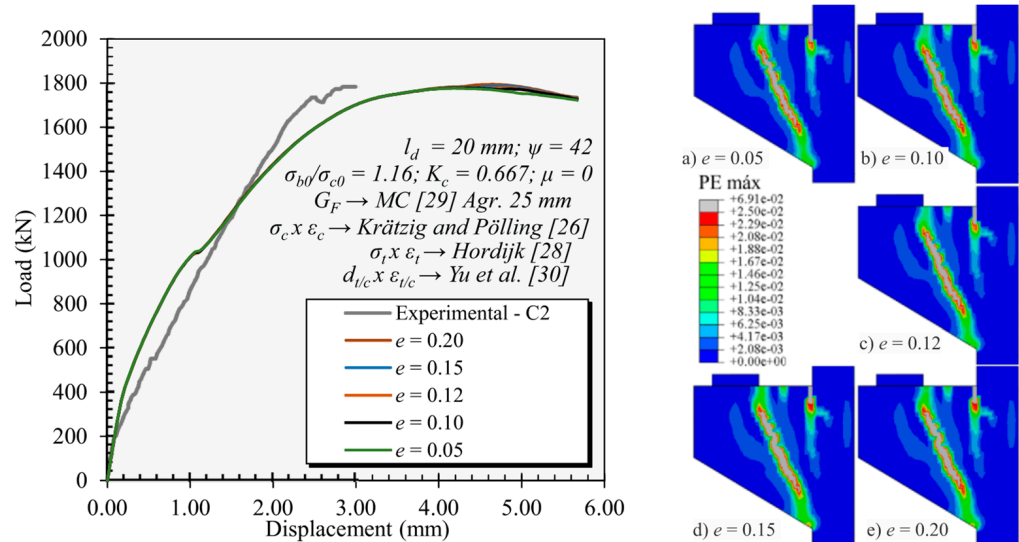


Figure 22. Influence of eccentricity (e) on load \times displacement behavior and cracking pattern of corbel C2 [26,28–30].

Figure 23 shows the numerical results of corbel C2 when varying the dilation angle from 30° to 45°. The changes in the load \times displacement curve occurred only after a load of 700 kN, at which plastification began in the central region of the strut as characterized by the first load drop in the graph. In general, higher values of dilation angle increased the load at which the plastification of the strut started and the ultimate capacity of the corbel. Comparing the cracking pattern of the numerical models showed that increasing the dilation angle from 30° to around 39° increased the region of plastic strains (indicating the wider influence zone of the strut) and higher plastic strains at the interface between the column and the corbel (the primary reinforcement zone). The best fit between the experimental and numerical load \times displacement graph was achieved with a dilation angle of 42 degrees.

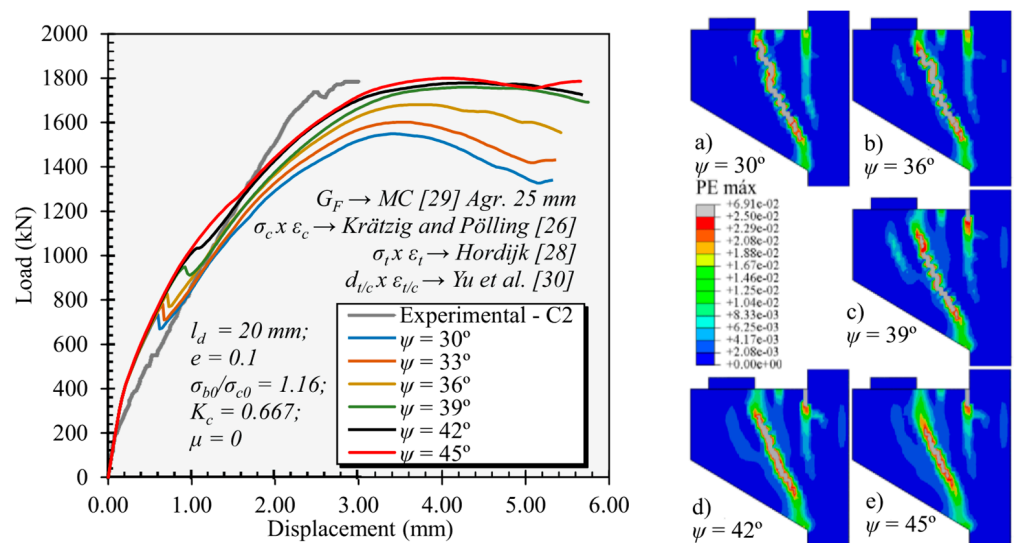


Figure 23. Influence of dilation angle (ψ) on the load \times displacement behavior and cracking pattern of corbel C2 [26,28–30].

6.6. Viscoplastic Regularization Parameter— μ

The viscosity (μ) is the numerical parameter related to time relaxation in the viscoplastic system used in the CDP model to overcome numerical convergence issues. In CDP, the viscosity value must be greater than or equal to zero. When $\mu = 0$, no viscoplastic regularization is considered. In the literature, viscosity values are frequently found between 10^{-3} [50], 10^{-4} [51], and 10^{-5} [12,43]. The default value considered for CDP is 0. In this work, viscosity values ranging from 0.01 to 0 were applied to investigate the influence of this parameter on the corbels.

Figure 24 shows the influence of varying the viscosity parameter in the numerical results for corbel C2. The load-displacement behavior and the cracking pattern using the viscosities 0, 10^{-6} , and 10^{-5} were coincident (the cracking pattern with $\mu = 10^{-6}$ was omitted in Figure 24).

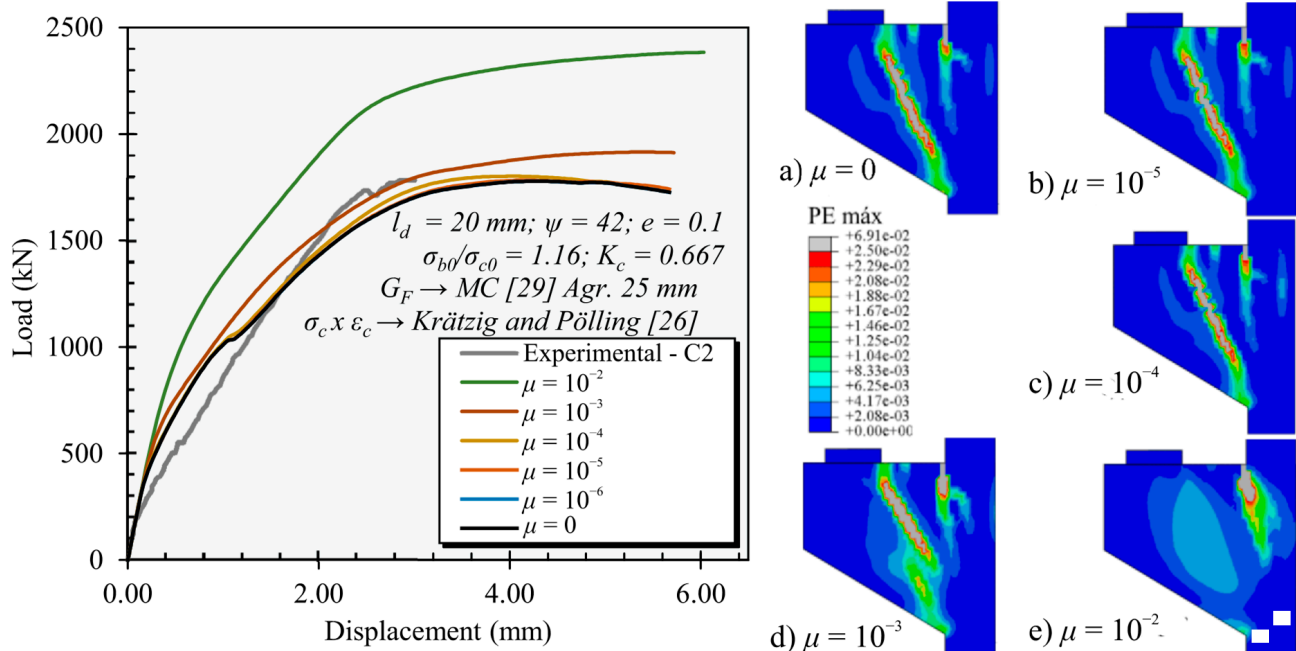


Figure 24. Influence of viscosity (μ) on the load vs. displacement behavior and cracking pattern of corbel C2 [26,29].

Increasing the viscosity μ to values $\geq 10^{-4}$ increased the ultimate capacity considerably. In addition, the cracking patterns for $\mu = 10^{-2}$ and $\mu = 10^{-3}$ indicated an overly large influence zone of the struts. This occurred because the residual tensile strength of the concrete was artificially increased (an undesired characteristic) by increasing the viscosity parameter [51]. Therefore, for values of viscosity between 10^{-2} and 10^{-3} , the material may redistribute the load similar to steel-fiber-reinforced concrete, which explains why the plastic strains were less concentrated at the strut region and covered a wider zone.

Michał and Andrzej [51] showed that increasing the viscosity value increases the damage distribution between the neighboring elements, which results in higher resistance of the structural member. Figure 25 shows the evolution of the tensile damage variable d_t (DAMAGET) with increasing viscosity values. In fact, with $\mu \geq 10^{-3}$, there was a larger spread of damage throughout the corbel, resulting in a higher ultimate capacity, as seen in Figure 24.

In order to overcome problems of convergence of the analysis, the computational cost of each viscosity value was also evaluated. When compared with the simulation with $\mu = 0$, the simulations with $\mu = 10^{-6}$ and $\mu = 10^{-5}$ did not show significant processing-time savings; whereas for $\mu = 10^{-4}$, $\mu = 10^{-3}$, and $\mu = 10^{-2}$, the computational cost reductions were 9%, 41%, and 44%, respectively.

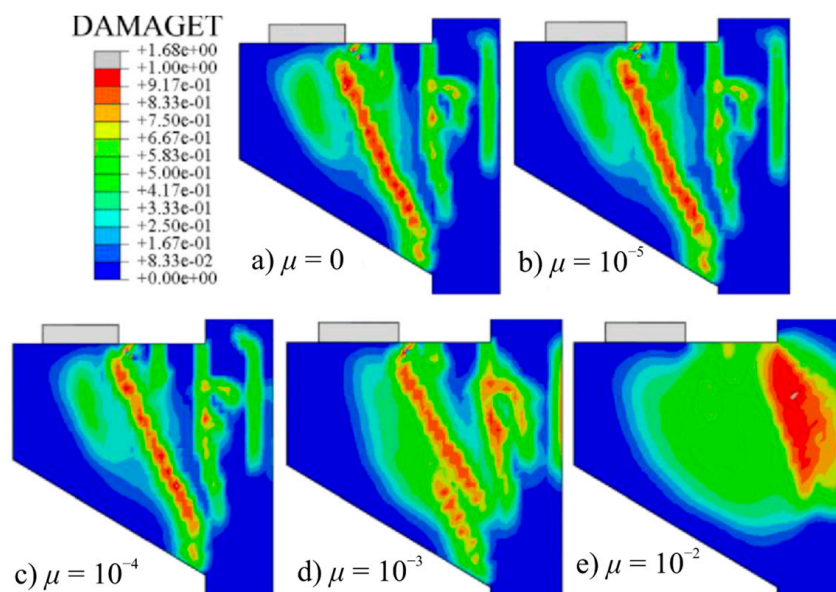


Figure 25. Influence of viscosity μ on the distribution of tensile damage in corbel C2.

7. Level of Accuracy for the Dataset

The proposed modeling choices to represent the non-linear response of the RC corbels were checked against a databank of 36 test results (4 from Wilson et al. [4] and 32 from other references that will be described in the next sections). In this way, the level of accuracy of the proposed framework for the NLFEA using CDP could be verified in detail.

7.1. Test by Khosravikia et al. [5]

Khosravikia et al. [5] tested three double corbels named S1, S2, and S3. The geometry of the corbels was similar to the corbels tested by Wilson et al. [4] (with $a/d = 0.59$ but with $b_w = 305$ mm). Details on the geometry and reinforcement layout can be consulted elsewhere [5].

The primary reinforcement of corbels S1 and S3 consisted of four bars with a diameter of 25.4 mm and yield strength of 471 MPa. In corbel S2, three bars with a diameter of 25.4 mm were adopted with a yield strength of 570 MPa. For the secondary reinforcement, in corbels S1 and S2, closed horizontal stirrups (a secondary reinforcement) and vertical ones with a diameter of 9.53 mm and a yield stress of 467 MPa were adopted. As for corbel S3, no secondary reinforcement was applied.

The concrete used in the corbels was designed to have a 28-day compressive strength of 34.5 MPa with a maximum aggregate size of $d_g = 10$ mm. Table 4 shows the compressive strength (f_{cm}), modulus of elasticity (E_c), and splitting tensile strength ($f_{tm,sp}$) on the day of the corbel test. The table also shows the direct tensile strength (f_{tm}) adopted in the numerical simulation of each corbel as well as the measured yield strength of reinforcement (f_{ym}).

Table 4. Material properties used for the corbels tested by Khosravikia et al. [5].

Property (MPa)		Testing Method	S1	S2	S3
Concrete	f_{cm} (MPa)	ASTM C39 [19]	27.1	26.5	27.3
	E_c (MPa)	ASTM C469 [20]	27,670	27,000	27,370
	$f_{tm,sp}$ (MPa)	ASTM C496 [21]	3.36	3.12	3.16
	f_{tm} (MPa)	$0.9f_{tm,sp}$	3.02	2.81	2.84
\varnothing 9.53 mm	f_{ym}	ASTM A370 [22]	467	467	-
\varnothing 25.4 mm	f_{ym} (MPa)		471	570	471

Figures 26–28 show the main test results and the predicted ones using NLFEA. In these figures, item (a) corresponds to the load vs. displacement behavior, highlighting points of interest such as the beginning of the first flexural cracks, the beginning of the inclined cracks in the strut, and the point corresponding to the ultimate failure load (the starting points of cracking in the S3 strut were not documented by the researchers). Items (b) and (c) are the maximum plastic deformations of the simulation at the instant of the ultimate load. Item (d) shows the tensile damage coefficient (d_t), and finally, items (e) and (f) correspond to the cracking evolution and the final cracking pattern of the tested corbels, respectively.

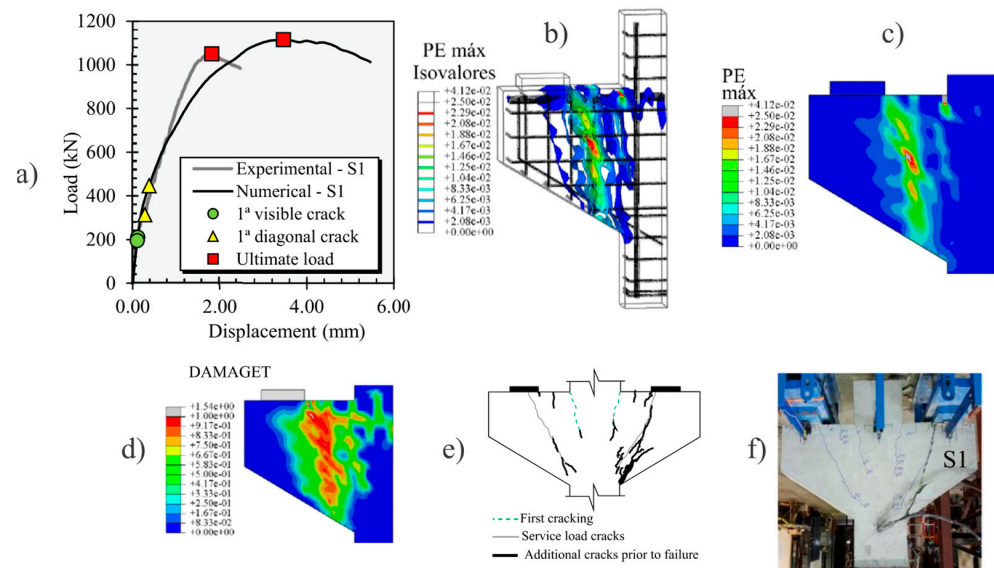


Figure 26. Experimental and numerical results for corbel S1 from Khosravikia et al. [5]: (a) load-displacement graphs; (b) distribution of inner cracking in the numerical model through isovalors of plastic strains; (c) distribution of maximum plastic strains at the corbel face; (d) distribution of tensile damage in the corbel face and (e) evolution of the cracking pattern at the test; (f) cracking pattern after failure.

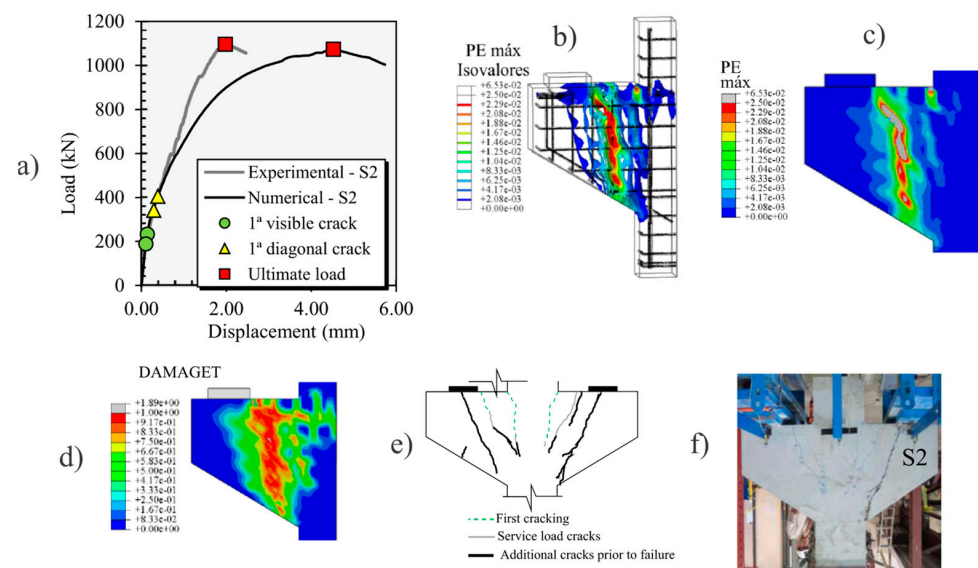


Figure 27. Experimental and numerical results for corbel S2 from Khosravikia et al. [5]: (a) load-displacement graphs; (b) distribution of inner cracking in the numerical model through isovalors of plastic strains; (c) distribution of maximum plastic strains at the corbel face; (d) distribution of tensile damage in the corbel face and (e) evolution of the cracking pattern at the test; (f) cracking pattern after failure.

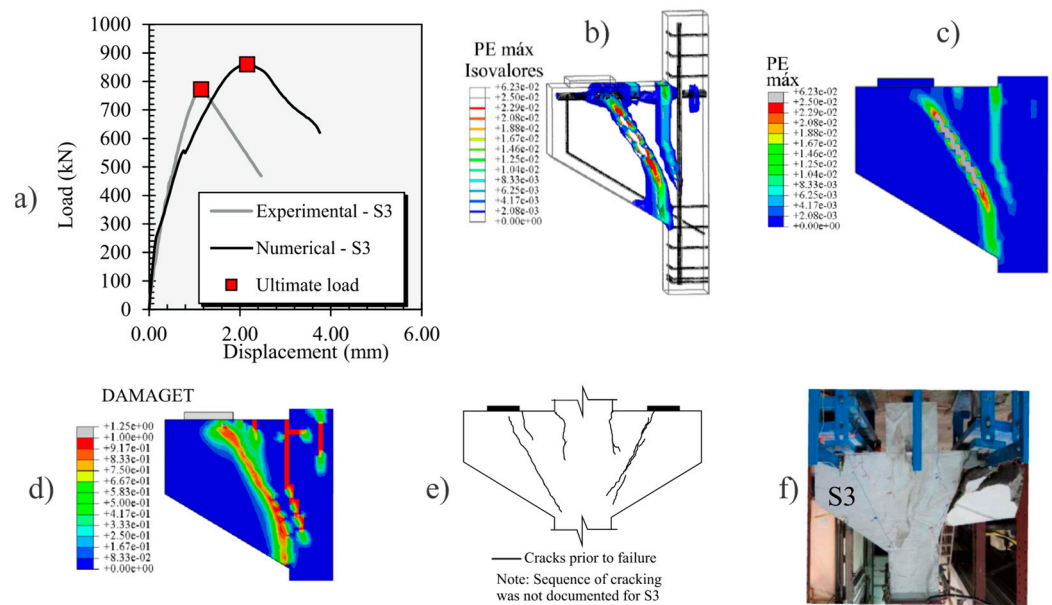


Figure 28. Experimental and numerical results for corbel S3 from Khosravikia et al. [5]: (a) load-displacement graphs; (b) distribution of inner cracking in the numerical model through isovalues of plastic strains; (c) distribution of maximum plastic strains at the corbel face; (d) distribution of tensile damage in the corbel face and (e) evolution of the cracking pattern at the test; (f) cracking pattern after failure.

As in the tested corbels, no reinforcement yielding was observed in the numerical models at failure. Therefore, failure of both the experimental and numerical corbels was governed by failure in the strut region.

The evolution of the cracking pattern was also well tracked by the numerical models: (i) firstly, flexural cracks appeared at the column–corbel interface, followed (ii) by the onset and propagation of inclined cracks in the region of the strut until the failure. The starting points of the flexural cracks in the experimental tests and in the numerical simulations were quite similar. Nevertheless, inclined cracks appeared at slightly higher loads in the numerical simulations when compared to the experimental tests. In general, the cracking patterns of the numerical simulations fitted well with those observed in the experimental tests.

For corbels S1 and S2, the differences between the predicted and tested ultimate loads were 6.2% and 2.1%, respectively. As for corbel S3, the predicted failure load was 11.4% higher than that of the experimental one.

7.2. Tests by Fattuhi

In Fattuhi [52], Fattuhi [53], Fattuhi and Hughes [54], and Hughes and Fattuhi [55], a variety of corbels with different geometries, reinforcement ratios, and concrete strengths with different fiber volumes were studied. Figure 29 shows the typical geometry used in these studies, for which the value of the load application distance (a) and the effective depth (d) are given in Table 5 for each corbel. It should be noted that the corbels selected in Table 5 were corbels composed of concrete without the presence of fibers. Note that the a/d ratio of the tests ranged from 0.41 to 1.46. Some more detailed information on the corbels tested by Fattuhi and Hughes [54] and Hughes and Fattuhi [55] is given in Canha et al. [6] and Naegeli [56].

Table 5 presents the material properties of the materials used in the numerical models. For the compressive strength of concrete (f_{cm}), the value measured on cube specimens was multiplied by 0.82 [39] to take into account the difference between the compressive tests using a cylindrical specimen (100×200) and a cubic specimen ($100 \times 100 \times 100$). For the corbels in Fattuhi [52] and Fattuhi [53], the tensile strength (f_{tm}) was multiplied by 0.9 to

consider the difference between the splitting tensile tests and direct tension [57]. For the corbels in Fattuhi and Hughes [54] and Hughes and Fattuhi [55], the tensile strength (f_{tm}) was estimated using the *fib* Model Code 2010 expression [24]:

$$f_{tm} = 0.3 \cdot (f_{cm} - 8)^{2/3} \quad (20)$$

According to the authors, the maximum aggregate size for the concrete was 10 mm. The concrete modulus of elasticity (E_c) of all corbels was estimated using the *fib* Model Code 2010 expression [24] with $\alpha_e = 1.0$:

$$E_c = (0.8 + 0.2 f_{cm}/88) \cdot 21,500 \cdot \alpha_e \cdot (f_{cm}/10)^{1/3} \quad (21)$$

Table 5 also describes the reinforcement used in each corbel. In the tested corbels that had three bars as a primary reinforcement, two bars with larger diameters were applied in the numerical corbels with the same total cross-sectional areas. It was observed that the T2 and T7 corbels had a secondary reinforcement (seam reinforcement), and the T8 and T9 corbels had two secondary reinforcements (seam reinforcements), both in the form of stirrups with two branches.

For the simulation, the corbels were discretized with an average size of finite elements (l_d) of 7.5 mm (Figure 29b), and a double symmetry of the corbels was adopted, as shown in Figure 29c. The displacement imposed on the RP-1 point was -3 mm in the y -direction. Figures 30–32 compare the experimental and numerical cracking patterns of corbels T6, 34, and 25, respectively. In general, the numerical model of corbel T6 accurately represented the cracking pattern evolution of the test, starting with the flexural cracks and finishing with a large inclined crack in the central region of the strut. For corbels 34 and 25, with an a/d of 1.11 and 0.89, respectively, an additional crack between the column and the support plate also arose in the numerical models and in the tests, which is very common in corbels with geometries closer to a beam.

In general, minor differences in inclinations of the cracks and load \times displacement graphs between the test and numerical results can be attributed to the isotropic material properties considered for the concrete in the numerical models as well as to the perfect adhesion assumed between the reinforcement and concrete. In practice, the material properties varied along the corbels, and cracks generally started at the weakest points. In addition, some bond-slip between the reinforcement and concrete could also change the global stiffness of the corbel and change the inclination of the cracks. Nevertheless, it was assumed that the main results of the numerical models (governing the failure mechanism and the ultimate loads) were accurately predicted.

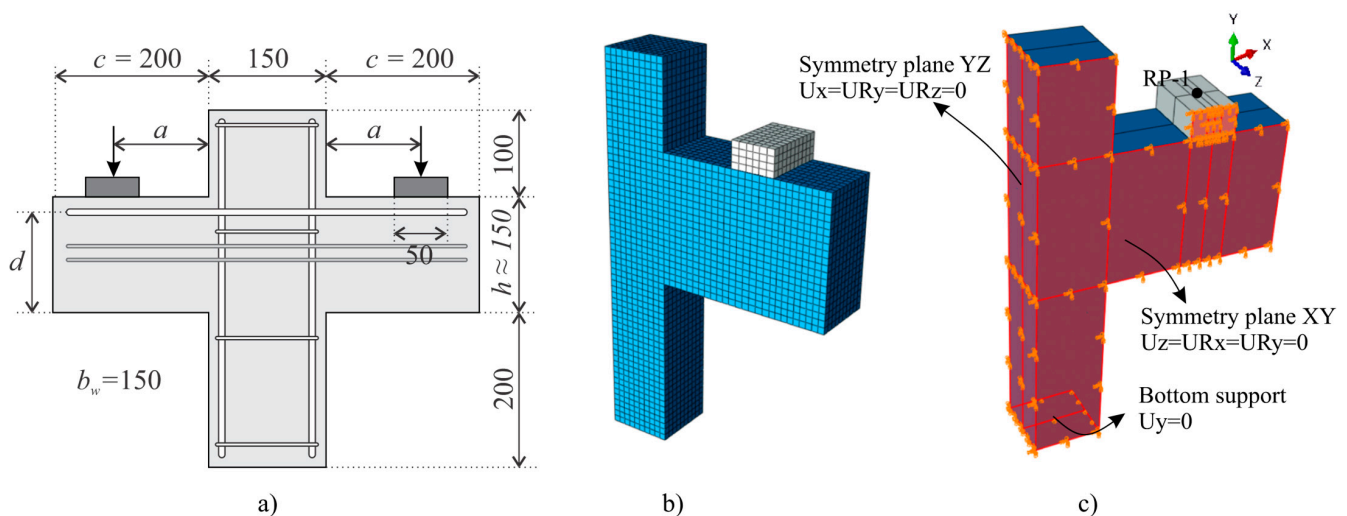


Figure 29. (a) Typical geometry of the corbels used in Fattuhi's studies; (b) mesh discretization with l_d of 7.5 mm; (c) boundary conditions of the corbels.

Table 5. Geometric properties, material properties, and reinforcement amounts of the corbels tested in Fattuhi's studies.

Corbel	<i>a</i> (mm)	<i>d</i> (mm)	<i>a/d</i>	<i>c</i> (mm)	<i>h</i> (mm)	<i>b_w</i> (mm)	<i>f_{cm}</i> (MPa)	<i>f_{tm}</i> (MPa)	<i>E_c</i> (MPa)	Quant.	ϕ (mm)	<i>d</i> (mm)	<i>f_y</i> (MPa)
Fattuhi [52]													
25	110	123	0.89	200	150	150	30.50	2.718	27,513.2	2	12	123	452
26	80	125	0.64	200	150	150	30.50	2.718	27,513.2	2	10	125	450
33	75	124	0.60	200	150	150	32.80	3.258	28,361.7	2	8	124	450
34	135	122	1.11	200	150	150	32.80	3.258	28,361.7	2 *	14.7 *	122	452
41	135	123	1.10	200	150	150	29.44	2.889	27,110.6	2 **	13.26 **	123	452
42	135	121	1.12	200	150	150	29.44	2.889	27,110.6	2	18	121	427
Fattuhi [53]													
65	110	91.8	1.20	200	147.8	150	28.29	3.024	26,670.2	2	12	91.8	452
66	135	93	1.45	200	149	150	28.29	3.024	26,670.2	2 *	14.7 *	93	452
67	110	132.4	0.83	200	148.4	150	30.012	3.159	27,328.1	2	12	132.4	452
68	110	112.4	0.98	200	148.4	150	30.012	3.159	27,328.1	2	12	112.4	452
69	135	122.6	1.10	200	148.6	150	26.24	2.799	25,864.9	2 *	14.7 *	122.6	452
70	135	92.3	1.46	200	148.3	150	26.24	2.799	25,864.9	2 *	14.7 *	92.3	452
71	110	121.5	0.91	200	147.5	150	28.29	2.79	26,670.2	2 **	13.26 **	121.5	452
72	110	123.2	0.89	200	149.2	150	28.29	2.79	26,670.2	2	12	123.2	452
73	75.0	124	0.60	200	148	150	28.29	2.898	26,670.2	2	8	124	451
74	75.0	94.2	0.80	200	148.2	150	28.29	2.898	26,670.2	2	8	94.2	451
Fattuhi and Hughes [54]													
T1	89	105	0.85	200	150	150	41.21	3.099	29,158.4	2	10	105	558
T2	89	130	0.68	200	150	150	41.21	3.099	29,158.4	2 2	10 10	130 76	558
T6	89	137	0.65	200	150	150	43.05	3.213	29,707.6	2	12	137	491
T7	89	130	0.68	200	150	150	39.46	2.990	28,629.5	2 2	12 10	130 80	491 558
T8	89	130	0.68	200	150	150	43.05	3.213	29,707.6	2 2 2	12 10 10	130 93 85	491 558 558
T9	89	130	0.68	200	150	150	39.46	2.990	28,629.5	2 2 2	12 10 10	130 69 61	491 558 558
Hughes and Fattuhi [55]													
C1	125	120	1.04	200	150	150	39.57	2.996	28,659.1	2	10	120	558
C21	53	129	0.41	200	150	150	38.75	2.944	28,391.6	2	8	129	495
C22	89	129	0.69	200	150	150	41.10	3.093	29,129.2	2	8	129	495
C23	125	129	0.97	200	150	150	41.10	3.093	29,129.2	2	8	129	495
C24	53	129	0.41	200	150	150	38.75	2.944	28,391.6	2	10	129	558
C25	65	129	0.50	200	150	150	40.80	3.074	29,041.6	2	12	129	491
C26	125	129	0.97	200	150	150	39.57	2.996	28,659.1	2	12	129	491

Notes: * 3 ϕ 12 mm; ** 1 ϕ 8 mm + 2 ϕ 12 mm.

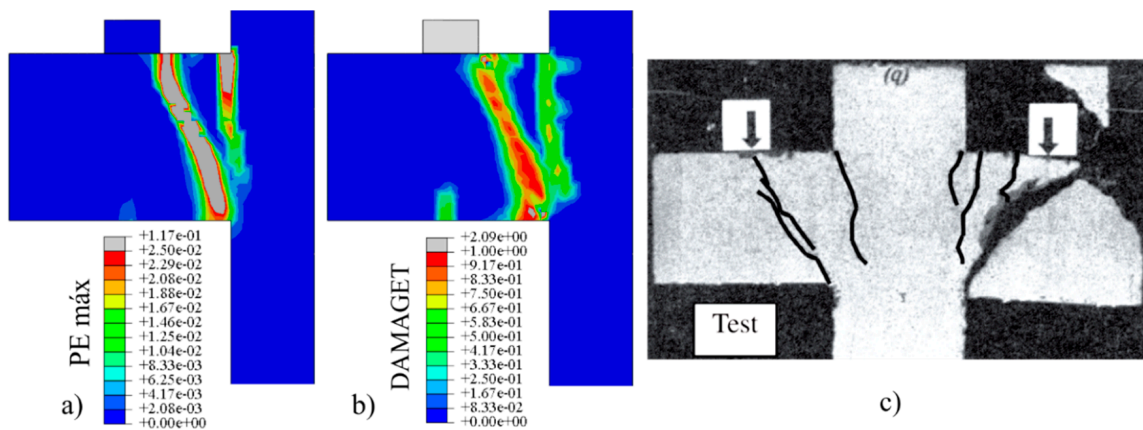


Figure 30. Comparison between the tested and predicted cracking pattern of corbel T6 at failure: (a) distribution of maximum tensile plastic strains; and (b) tensile damage in the numerical model; (c) cracking pattern after failure in the test.

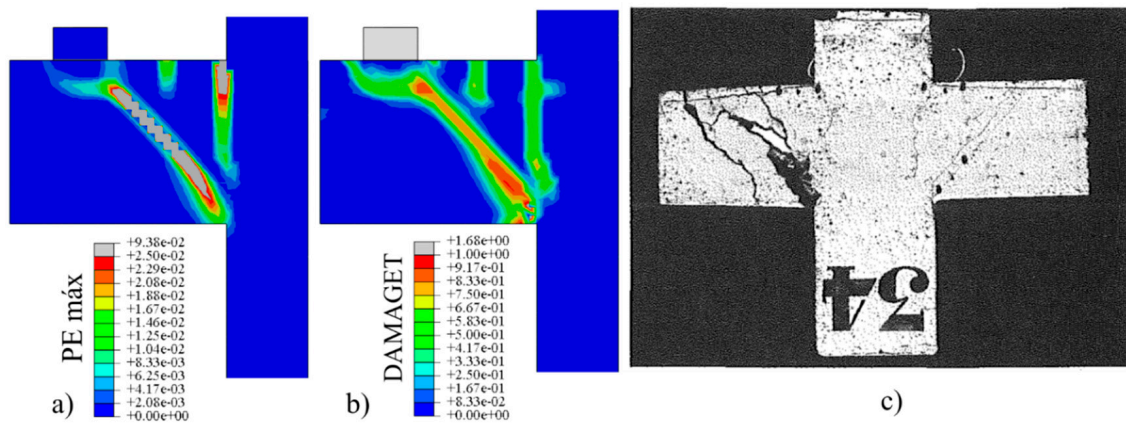


Figure 31. Comparison between the tested and predicted cracking pattern of corbel 34 at failure: (a) distribution of maximum tensile plastic strains; and (b) tensile damage in the numerical model; (c) cracking pattern after failure in the test.

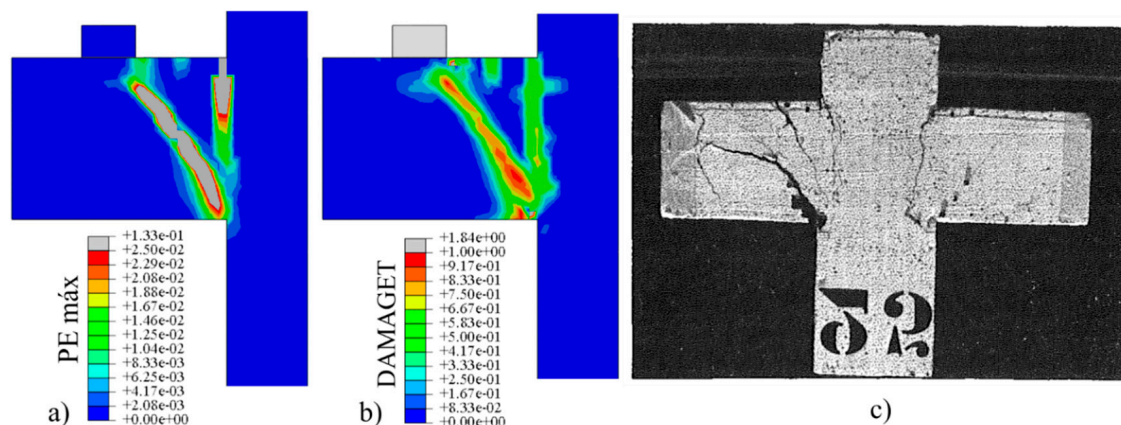


Figure 32. Comparison between the tested and predicted cracking pattern of corbel 25 at failure: (a) distribution of maximum tensile plastic strains; and (b) tensile damage in the numerical model; (c) cracking pattern after failure in the test.

7.3. Summary of the Accuracy Level of the NLFEA

Table 6 presents a comparison between the ultimate loads observed in the tests (F_{EXP}) and the predicted ones with the proposed framework for the NLFEA (F_{FEM}). The mean

ratio between the numerical and experimental failure loads F_{FEM}/F_{EXP} was 1.015 with a coefficient of variation equal to 8.57%. Therefore, the proposed framework for the NLFEA provided accurate predictions of the ultimate load for the databank, similar to the ones achieved in other studies related to RC corbels using NLFEA [5–7]. For instance, the ratio between the predicted and tested resistances in Khosravikia et al. [5] was 0.972 with a coefficient of variation equal to 9.35%. In Canha et al. [6], the average ratio between the tested and predicted resistances for the simulated corbels was 1.03 with a coefficient of variation equal to 15.9%. In both publications, two-dimensional NLFEA was employed. Therefore, this work also showed that the level of accuracy using two-dimensional or three-dimensional NLFEA provides similar levels of accuracy for RC corbels. Nevertheless, the proposed 3D modeling approach is the most flexible because it may be used to investigate the effect of load eccentricity along the corbel width, for instance.

Table 6. Comparison between experimental (tested) and predicted resistances and failure mechanism with the finite element models (FEMs). FME = failure mode in the experiment; FMF = failure mode in the finite element model; C = failure in the strut; T = failure at the primary reinforcement; CP = whether the failure mechanism was correctly predicted.

Reference	Corbel	a/d	f_{cm} (MPa)	F_{EXP} (kN)	F_{FEM} (kN)	F_{FEM}/F_{EXP}	FME	FMF	CP
Wilson et al. [4]	C0	0.66	36.54	1426.2	1458.0	1.02	C	T	No
	C1	0.59	44.82	1677.7	1627.2	0.97	T	T	Yes
	C2	0.59	46.88	1784.5	1778.2	1.00	T	T	Yes
	C3	0.59	38.61	1544.2	1346.9	0.87	T	T	Yes
Khosravikia et al. [5]	S1	0.59	27.10	1050.0	1115.4	1.06	C	C	Yes
	S2	0.59	26.50	1096.5	1073.4	0.98	C	C	Yes
	S3	0.59	27.30	772.0	860.1	1.11	C	C	Yes
Fattuhi [52]	25	0.89	30.50	108.5	103.1	0.95	T	T	Yes
	26	0.64	30.50	112.5	114.8	1.02	T	T	Yes
	33	0.60	32.80	91	85.3	0.94	T	T	Yes
	34	1.11	32.80	114	104.1	0.91	T	T	Yes
	41	1.10	29.44	98	92.2	0.94	T	T	Yes
	42	1.12	29.44	111.5	99.1	0.89	C	C	Yes
Fattuhi [53]	65	1.20	28.29	74	82.1	1.11	T	T	Yes
	66	1.45	28.29	73.5	70.7	0.96	T	T	Yes
	67	0.83	30.01	101.3	100.9	1.00	T	T	Yes
	68	0.98	30.01	96	95.0	0.99	T	T	Yes
	69	1.10	26.24	93.5	89.2	0.95	C	T	No
	70	1.46	26.24	67.3	65.9	0.98	C	C	Yes
	71	0.91	28.29	116.5	110.5	0.95	T	T	Yes
	72	0.89	28.29	101	93.3	0.92	T	T	Yes
	73	0.60	28.29	87.5	83.5	0.95	T	T	Yes
74	0.80	28.29	74.3	63.5	0.86	T	T	Yes	
Fattuhi and Hughes [54]	T1	0.85	41.21	93	100.0	1.08	C	C	Yes
	T2	0.68	41.21	146	156.4	1.07	C	T	No
	T6	0.65	43.05	136	138.0	1.01	T	T	Yes
	T7	0.68	39.46	157	169.7	1.08	C	C	Yes
	T8	0.68	43.05	188	212.3	1.13	T	T	Yes
	T9	0.68	39.46	153	179.9	1.18	C	C	Yes
Hughes and Fattuhi [55]	C1	1.04	39.57	80	88.2	1.10	C	C	Yes
	C21	0.41	38.75	114	123.2	1.08	T	T	Yes
	C22	0.69	41.10	82	81.5	0.99	T	T	Yes
	C23	0.97	41.10	47	58.0	1.23	T	T	Yes
	C24	0.41	38.75	145	151.0	1.04	C	T	No
	C25	0.50	40.80	151	159.3	1.06	T	T	Yes
	C26	0.97	39.57	90	102.0	1.13	C	C	Yes
Average						1.015			32/36
Standard deviation						0.087			
Coefficient of variation						8.57%			

Different from previous publications in this field [5,6], we also attempted to highlight the level of accuracy related to the prediction of the governing failure mechanism. Table 5 shows that the governing failure mechanism, either concrete crushing at the strut (C) or

reinforcement yielding of the primary reinforcement (T), was also well predicted by the numerical models. The governing failure mechanism was correctly predicted in 32/36 = 88% of the tests using the numerical models.

8. Conclusions

In this study, the behavior of reinforced concrete corbels was evaluated through advanced non-linear finite element analysis. Firstly, the proposed framework for the non-linear finite element analysis was checked against a specific experimental program. Afterwards, a sensibility study was conducted to show the parameters of the Concrete Damaged Plasticity model that more significantly influenced the ultimate capacity and deformation capacity of the corbels. In the end, the proposed approach to the NLFEA using CDP was checked against a databank of 36 test results. The following conclusions could be drawn:

- The shape factor K_c , the dilation angle ψ , and the viscosity parameter μ were the most influential parameters in the deformation and ultimate capacity of the numerical models of the RC corbels. After proper calibration, the chosen parameter values were allowed to accurately represent a reasonable number of test results from the literature.
- Values of viscosity parameters higher than 10^{-4} should be avoided because they significantly change the cracking pattern evolution and the corresponding ultimate capacity of the corbels. In practice, such values may increase the residual tensile and compressive strength of concrete and induce a larger influence zone for the cracks, changing the governing failure mechanisms of the numerical models.
- Different stress–strain behavior models in compression did not significantly change the ultimate capacity of the modeled corbels. This indicates that in practice, the tensile cracks also govern the capacity of the struts.
- The proposed framework for the NLFEA of reinforced concrete corbels was able to satisfactorily predict the global behavior of corbels with different geometries with an a/d varying from 0.4 to 1.4 and a compressive strength of concrete of 28 to 46 MPa.
- The numerical models allowed the accurate prediction of the ultimate loads of RC corbels with varied geometries and material properties. The average ratio between the predicted and tested resistances was 1.015 with a coefficient of variation of 8.57% for the databank, including 36 test results from the literature.
- Different failure mechanisms may govern the ultimate limit states of RC corbels. In this context, the proposed modeling approach allowed the correct prediction of the governing failure mechanism for approximately 88% of the test results. Therefore, an NLFEA can be used not only to assess the ultimate capacity but also to guide eventual strengthening tasks in existing corbels to indicate whether the primary reinforcement or the strut capacity should be improved.

Author Contributions: Conceptualization, L.R., A.M.D.d.S. and M.K.E.D.; methodology, L.R. and A.M.D.d.S.; software, L.R.; validation, L.R.; formal analysis, L.R.; investigation, L.R.; resources, L.R., A.M.D.d.S. and M.K.E.D.; data curation, L.R. and A.M.D.d.S.; writing—original draft preparation, A.M.D.d.S. and J.V.C.S.; writing—review and editing, L.R., A.M.D.d.S. and J.V.C.S.; visualization, L.R.; supervision, M.K.E.D.; project administration, M.K.E.D.; funding acquisition, M.K.E.D. All authors have read and agreed to the published version of the manuscript.

Funding: The authors acknowledge the financial support provided by the São Paulo Research Foundation (FAPESP) under grant number #2021/13916-0 and by the Brazilian National Council for Scientific and Technological Development (CNPq) under grant number #303438/2016-9. This study was also financed in part by the Coordenação de Aperfeiçoamento de Pessoal de Nível Superior—Brasil (CAPES) under Finance Code 001.

Data Availability Statement: Others that support the findings of this study are available from the first author (L.R.) upon reasonable request.

Conflicts of Interest: The authors declare no conflict of interest.

References

1. Shu, J. Shear assessment of a reinforced concrete bridge deck slab according to level-of-approximation approach. *Struct. Concr.* **2018**, *19*, 1838–1850. [[CrossRef](#)]
2. Lantsoght, E.O.L.; de Boer, A.; van der Veen, C. Distribution of peak shear stress in finite element models of reinforced concrete slabs. *Eng. Struct.* **2017**, *148*, 571–583. [[CrossRef](#)]
3. De Sousa, A.M.D.; Lantsoght, E.O.L.; El Debs, M.K. Failure mechanism of one-way slabs under concentrated loads after local reinforcement yielding. *Eng. Struct.* **2023**, *291*, 116396. [[CrossRef](#)]
4. Wilson, H.R.; Yousefpour, H.; Brown, M.D.; Bayrak, O. Investigation of Corbels Designed According to Strut-and-Tie and Empirical Methods. *ACI Struct. J.* **2018**, *115*, 813–824. [[CrossRef](#)]
5. Khosravikia, F.; Kim, H.S.; Yi, Y.; Wilson, H.; Yousefpour, H.; Hrynyk, T.; Bayrak, O. Experimental and Numerical Assessment of Corbels Designed Based on Strut-and-Tie Provisions. *J. Struct. Eng.* **2018**, *144*, 04018138. [[CrossRef](#)]
6. Canha, R.M.F.; Kuchma, D.A.; El Debs, M.K.; de Souza, R.A. Numerical analysis of reinforced high strength concrete corbels. *Eng. Struct.* **2014**, *74*, 130–144. [[CrossRef](#)]
7. de Lima Araújo, D.; Azevedo Coelho, S.; Regina Mesquita de Almeida, S.; Khalil El Debs, M. Computational modelling and analytical model for two-step corbel for precast concrete system. *Eng. Struct.* **2021**, *244*, 112699. [[CrossRef](#)]
8. Neuberger, Y.M.; Araújo, D.d.L. An improved analytical model for two-step corbels in a precast concrete system. *Eng. Struct.* **2023**, *284*, 115947. [[CrossRef](#)]
9. Beshara, F.; Mustafa, T.; Mahmoud, A.; Khalil, M. Constitutive models for nonlinear analysis of SFRC corbels. *J. Build. Eng.* **2020**, *28*, 101092. [[CrossRef](#)]
10. Syroka, E.; Bobiński, J.; Tejchman, J. FE analysis of reinforced concrete corbels with enhanced continuum models. *Finite Elem. Anal. Des.* **2011**, *47*, 1066–1078. [[CrossRef](#)]
11. Genikomsou, A.S.; Polak, M.A. Finite element analysis of punching shear of concrete slabs using damaged plasticity model in ABAQUS. *Eng. Struct.* **2015**, *98*, 38–48. [[CrossRef](#)]
12. De Sousa, A.M.; Lantsoght, E.O.; Genikomsou, A.S.; Krahl, P.A.; El Debs, M.K. Behavior and punching capacity of flat slabs with the rational use of UHPFRC: NLFEA and analytical predictions. *Eng. Struct.* **2021**, *244*, 112774. [[CrossRef](#)]
13. Lubliner, J.; Oliver, J.; Oller, S.; Oñate, E. A plastic-damage model for concrete. *Int. J. Solids Struct.* **1989**, *25*, 299–326. [[CrossRef](#)]
14. Lee, J.; Fenves, G.L. Plastic-Damage Model for Cyclic Loading of Concrete Structures. *J. Eng. Mech.* **1998**, *124*, 892–900. [[CrossRef](#)]
15. Dassault Systems Simulia Corp. *Abaqus Analysis User's Manual 6.14*; Dassault Systems Simulia Corp.: Providence, RI, USA, 2014.
16. Cheng, H.; Paz, C.M.; Pinheiro, B.C.; Estefen, S.F. Experimentally based parameters applied to concrete damage plasticity model for strain hardening cementitious composite in sandwich pipes. *Mater. Struct./Mater. Constr.* **2020**, *53*, 78. [[CrossRef](#)]
17. Krahl, P.A.; Carrazedo, R.; El Debs, M.K. Mechanical damage evolution in UHPFRC: Experimental and numerical investigation. *Eng. Struct.* **2018**, *170*, 63–77. [[CrossRef](#)]
18. ACI Committee 318. *Building Code Requirements for Structural Concrete (ACI 318-14) and Commentary*; American Concrete Institute: Indianapolis, IN, USA, 2014; Volume 11, p. 6858.
19. *ASTM C39/C39M-17*; Standard Test Method for Compressive Strength of Cylindrical Concrete Specimens. ASTM International: West Conshohocken, PA, USA, 2017.
20. *ASTM C469/469M-14*; Standard Test Method for Static Modulus of Elasticity and Poisson's Ratio of Concrete in Compression. ASTM International: West Conshohocken, PA, USA, 2014.
21. *ASTM C496/C496M-04*; Standard Test Method for Splitting Tensile Strength of Cylindrical Concrete Specimens. ASTM International: West Conshohocken, PA, USA, 2004.
22. *ASTM A370-17*; Standard Test Methods and Definitions for Mechanical Testing of Steel Products. ASTM International: West Conshohocken, PA, USA, 2017.
23. Milligan, G.J.; Polak, M.A.; Zurell, C. Impact of Column Rectangularity on Punching Shear Strength: Code Predictions versus Finite Element Analysis. *J. Struct. Eng.* **2021**, *147*, 04020331. [[CrossRef](#)]
24. Fédération Internationale du Béton (fib). *fib Model Code for Concrete Structures 2010*; Bulletin 65; Ernst & Sohn-Fédération Internationale Du Béton: Lausanne, Switzerland, 2012; Volume 1–2.
25. *EN 1992-1-1:2004 2004*; EN 1992-1-1: Eurocode 2: Design of Concrete Structures -Part 1-1: General Rules and Rules for Buildings. CEN: Brussels, Belgium, 2004.
26. Krätzig, W.B.; Pölling, R. An elasto-plastic damage model for reinforced concrete with minimum number of material parameters. *Comput. Struct.* **2004**, *82*, 1201–1215. [[CrossRef](#)]
27. Oller, S. A continuous Damage Model for Frictional Materials. Ph.D. Thesis, Technical University of Catalonia, Barcelona, Spain, 1988. (In Spanish)
28. Hordijk, D.A. *Tensile and Tensile Fatigue Behaviour of Concrete—Experiments, Modelling and Analyses*; Heron: Dronfield, UK, 1992; Volume 37, pp. 3–79.
29. Comité Euro-International du Béton. *CEB-FIP Model Code 1990: Design Code*; Comité Euro-International du Béton: Luxembourg, 1993. [[CrossRef](#)]
30. Yu, T.; Teng, J.G.; Wong, Y.L.; Dong, S.L. Finite element modeling of confined concrete-II: Plastic-damage model. *Eng. Struct.* **2010**, *32*, 680–691. [[CrossRef](#)]
31. Kupfer, H.B.; Gerstle, K.H. Behavior of Concrete under Biaxial Stresses. *J. Eng. Mech. Div.* **1973**, *99*, 853–866. [[CrossRef](#)]

32. Kupfer, H.B.; Hilsdorf, H.K.; Rusch, H. Behavior of Concrete Under Biaxial Stresses. *ACI J. Proc.* **1969**, *66*, 656–666. [[CrossRef](#)]
33. Wiliam, K.; Warnke, E. *Constitutive Model for the Triaxial Behaviour of Concrete*. Seminar on Concrete Structures Subjected to Triaxial Stresses; ISMES: Bergamo, Italy, 1974; pp. 1–30.
34. Gonzalez-Vidoso, F.; Kotsovos, M.D.; Pavlovic, M.N. Symmetrical Punching of Reinforced Concrete Slabs: An Analytical Investigation Based on Nonlinear Finite Element Modeling. *Struct. J.* **1988**, *85*, 241–250. [[CrossRef](#)]
35. Meng, B.; Li, F.; Zhong, W.; Zheng, Y.; Du, Q. Strengthening strategies against the progressive collapse of steel frames with extended end-plate connections. *Eng. Struct.* **2023**, *274*, 115154. [[CrossRef](#)]
36. Nana, W.; Bui, T.; Limam, A.; Abouri, S. Experimental and Numerical Modelling of Shear Behaviour of Full-Scale RC Slabs under Concentrated Loads. *Structures* **2017**, *10*, 96–116. [[CrossRef](#)]
37. de Sousa, A.M.D.; Lantsoght, E.O.L.; El Debs, M.K. Transition Between Shear and Punching in Reinforced Concrete Slabs: Review and Predictions with ACI Code Expressions. *ACI Struct. J.* **2023**, *120*, 115–128. [[CrossRef](#)]
38. de Sousa, A.M.D.; Lantsoght, E.O.L.; El Debs, M.K. Shear and Punching Capacity Predictions for One-Way Slabs under Concentrated Loads Considering the Transition between Failure Mechanisms. *Buildings* **2023**, *13*, 434. [[CrossRef](#)]
39. de Sousa, A.M.D.; Lantsoght, E.O.L.; Yang, Y.; El Debs, M.K. Extended CSDT model for shear capacity assessments of bridge deck slabs. *Eng. Struct.* **2021**, *234*, 111897. [[CrossRef](#)]
40. De Sousa, A.M.D.; Lantsoght, E.O.L.; El Debs, M.K. One-way shear strength of wide reinforced concrete members without stirrups. *Struct. Concr.* **2020**, *22*, 968–992. [[CrossRef](#)]
41. Guo, Z. Principles of Reinforced Concrete Design. *Princ. Reinf. Concr.* **2014**, *587*, 89–112. [[CrossRef](#)]
42. Birtel, V.; Mark, P. Parameterised Finite Element Modelling of RC Beam Shear Failure. In Proceedings of the Abaqus User’s Conference, Boston, MA, USA, 23–25 May 2006; pp. 95–108.
43. Santos, D.P.d.; Fernandes Neto, J.A.D.; Reginato, L.; Carrazedo, R. Optimized design of RC deep beams based on performance metrics applied to strut and tie model and in-plane stress conditions. *Lat. Am. J. Solids Struct.* **2019**, *16*, 212. [[CrossRef](#)]
44. Alfarah, B.; López-Almansa, F.; Oller, S. New methodology for calculating damage variables evolution in Plastic Damage Model for RC structures. *Eng. Struct.* **2017**, *132*, 70–86. [[CrossRef](#)]
45. Feenstra, P.H.; de Borst, R. Constitutive Model for Reinforced Concrete. *J. Eng. Mech.* **1995**, *121*, 587–595. [[CrossRef](#)]
46. Carreira, D.J.; Chu, K.H. Stress-strain relationship for plain concrete in compression. *ACI J.* **1985**, *82*, 797–804.
47. Cantone, R.; Ruiz, M.F.; Muttoni, A. Shear force redistributions and resistance of slabs and wide beams. *Struct. Concr.* **2021**, *22*, 2443–2465. [[CrossRef](#)]
48. Setiawan, A.; Vollum, R.L.; Macorini, L.; Izzuddin, B.A. Punching of RC slabs without transverse reinforcement supported on elongated columns. *Structures* **2020**, *27*, 2048–2068. [[CrossRef](#)]
49. Earij, A.; Alfano, G.; Cashell, K.; Zhou, X. Nonlinear three-dimensional finite-element modelling of reinforced-concrete beams: Computational challenges and experimental validation. *Eng. Fail. Anal.* **2017**, *82*, 92–115. [[CrossRef](#)]
50. Wosatko, A.; Winnicki, A.; Polak, M.A.; Pamin, J. Role of dilatancy angle in plasticity-based models of concrete. *Arch. Civ. Mech. Eng.* **2019**, *19*, 1268–1283. [[CrossRef](#)]
51. Michał, S.; Andrzej, W. Calibration of the CDP model parameters in Abaqus. In Proceedings of the 2015 World Congress on Advances in Structural Engineering and Mechanics (ASEM15), Incheon, Republic of Korea, 24–28 September 2015.
52. Fattuhi, N.I. Strength of SFRC Corbels Subjected to Vertical Load. *J. Struct. Eng.* **1990**, *116*, 701–718. [[CrossRef](#)]
53. Fattuhi, N.I. Strength of FRC Corbels in Flexure. *J. Struct. Eng.* **1994**, *120*, 360–377. [[CrossRef](#)]
54. Fattuhi, N.I.; Hughes, B.P. Ductility of Reinforced Concrete Corbels Containing Either Steel Fibers or Stirrups. *ACI Struct. J.* **1989**, *86*, 644–651. [[CrossRef](#)]
55. Hughes, B.P.; Fattuhi, N.I. Reinforced steel and polypropylene fibre concrete corbel tests. *Struct. Eng.* **1989**, *67*, 68–72.
56. Naegeli, C.H. *Estudo de Consolos de Concreto Armado*; Universidade Federal do Rio de Janeiro: Rio de Janeiro, Brazil, 1997.
57. *ABNT NBR 6118*. *NBR 6118*; Design of concrete structures—Procedure. Associação Brasileira de Normas Técnicas (ABNT): Rio de Janeiro, Brazil, 2014. (In Portuguese)

Disclaimer/Publisher’s Note: The statements, opinions and data contained in all publications are solely those of the individual author(s) and contributor(s) and not of MDPI and/or the editor(s). MDPI and/or the editor(s) disclaim responsibility for any injury to people or property resulting from any ideas, methods, instructions or products referred to in the content.